Department of Precision and Microsystems Engineering

Cerebral Blood Flow Measurement by Laser

Xuzhen You

Report no : 2025.041
Coach : Binbin Zhang
Professor : Nandini Bhattacharya
Specialisation : Optics for Technology (OPT)
Type of report : Master Thesis
Date : 20 August 2025

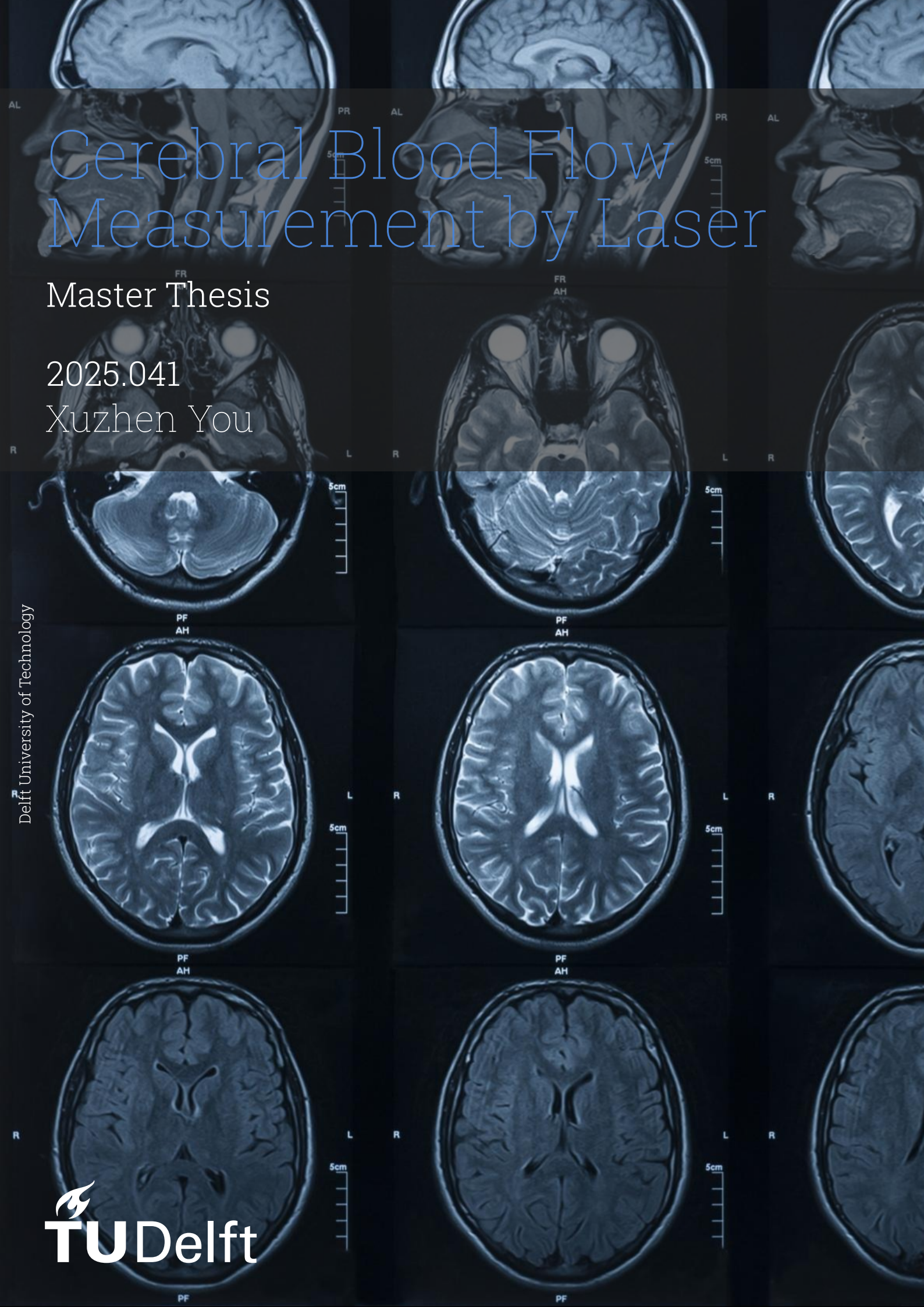

Cerebral Blood Flow Measurement by Laser

Master Thesis

2025.041

Xuzhen You

Delft University of Technology

TU Delft

Cerebral Blood Flow Measurement by Laser

Master Thesis

by

Xuzhen You

Instructor:	Binbin Zhang
	Dr. Nandini Bhattacharya
Project Duration:	Sep. 2024 - Aug. 2025
Institution:	Delft University of Technology
Faculty:	Department of Precision and Microsystems Engineering, Delft

TU Delft

Preface

As my time at Delft University of Technology draws to a close, I bid farewell to this beautiful city with deep appreciation for the journey it has offered. I would like to extend my heartfelt gratitude to all those who have supported and guided me throughout this project.

I am sincerely grateful to my supervisor, Dr. Nandini Bhattacharya, and to Binbin Zhang for their insightful advice, patient guidance, and unwavering support throughout the research process. Their prudence and encouragement have been instrumental in shaping and improving this thesis.

Finally, my deepest thanks go to my family and friends for their unconditional support and constant encouragement during my entire Master's project.

Xuzhen You
Delft, August 2025

Abstract

Cerebral blood flow (CBF) is a valuable physiological parameter for the diagnosis of brain function and disease. A number of optical techniques have been developed to estimate CBF non-invasively with high spatial and temporal resolutions with the benefit that no contrast dyes or surgical procedures are required.

In this project, we present a novel coherence-gated iSVS approach that leverages a low-cost, low-coherence laser diode to selectively filter out photons from superficial layers—eliminating the need for long SD separations. This strategy dramatically improves light throughput and spatial resolution while reducing system cost. Our method offers a practical and scalable solution for high-resolution, depth-sensitive CBF imaging.

To validate the system, experiments were performed using tissue-mimicking phantoms, where a programmable pump generated controlled flow patterns. The results demonstrate the technique's potential for high-resolution, real-time assessment of cerebral hemodynamics, offering a promising tool for both clinical and research applications.

Keywords: cerebral blood flow, iSVS, LSCI, time-of-flight gating, neurovascular imaging, speckle visibility, deep tissue imaging

Contents

Preface i

Summary ii

1 Introduction 1

2 Theory 3
2.1 Holography . . . 3
2.2 Time-Gated Imaging . . . 5
2.3 Laser Speckle Contrast Imaging (LSCI) . . . 5
2.4 Interferometric Speckle Visibility Spectroscopy (iSVS) . . . 7

3 Methods 10
3.1 Coherence Length Experiment . . . 10
3.1.1 Principle . . . 10
3.1.2 Methodology . . . 11
3.2 Tissue-mimicking Phantoms . . . 12
3.3 On-axis Configuration . . . 14
3.3.1 Principle . . . 14
3.3.2 Experimental arrangement . . . 15
3.4 Off-axis Configuration . . . 16
3.4.1 Principle . . . 17
3.4.2 Experimental arrangement . . . 18

4 Results 21
4.1 On-axis Configuration . . . 22
4.2 Off-axis Configuration . . . 25
4.2.1 Discussion . . . 30

5 Conclusion 32

References 34

A Source Code 36

B Figures 40

1

Introduction

Cerebral blood flow (CBF) is tightly regulated to meet the metabolic demands associated with brain activity. It ensures the delivery of oxygen and nutrients while facilitating the removal of waste products and heat. Disruptions in CBF are implicated in various neurological disorders, including stroke and Alzheimer's disease [1]. Therefore, the implementation of quantitative and localized measurements of CBF holds significant promise for advancing our understanding of major cerebrovascular diseases.

In recent decades, advances in laser technology and photonics have led to substantial progress in developing novel optical imaging and microscopy techniques for the in vivo quantification of blood flow. Compared to traditional angiographic modalities, optical techniques such as Interferometric Diffusing Wave Spectroscopy (iDWS) [2] offer non-invasive and cost-effective solutions for CBF measurement. Furthermore, these techniques show potential for integration into portable platforms, enabling real-time functional imaging of cerebral blood flow.

However, measuring CBF using optical devices remains challenging—primarily due to the difficulty of accessing and isolating brain signals, particularly within the constraints of biomedical safety regulations that limit exposure levels. This difficulty arises from the complex interactions between photons and biological tissues. As photons travel through tissue, they experience substantial scattering due to the heterogeneous composition of components such as cells, extracellular matrices, and blood vessels.

Monte Carlo simulations (figure 1.1) offer a powerful computational framework to address this challenge [3]. These simulations model photon transport in scattering media by tracing individual photon trajectories through virtual tissue models, accounting for both scattering and absorption properties.

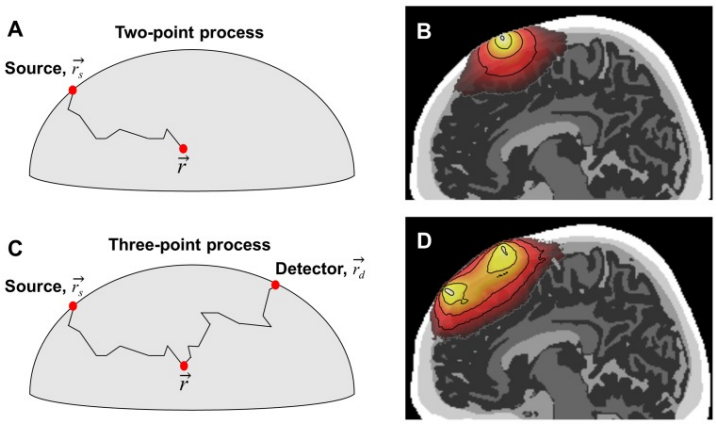

Figure 1.1: Monte Carlo simulations of different models [3]

Despite these computational advances, the practical implementation of optical CBF measurement con-

tinues to face challenges, including low signal-to-noise ratio (SNR), interference from superficial layers (scalp and skull), and susceptibility to motion artefacts.

Blood flow (BF) estimation can be achieved through two main sampling techniques: temporal and spatial. The temporal approach, known as time-domain diffuse correlation spectroscopy, analyzes the temporal ensemble of the speckle field. It typically uses a high-speed detector—often operating at frame rates above 100 kHz to monitor a single speckle or a small group of speckles [4].

In contrast, the spatial sampling technique, derived from laser speckle contrast imaging (LSCI), relies on the spatial ensemble of the speckle field. Rather than requiring a high-speed detector, it utilizes a camera with a wide detection area and a high number of pixels, allowing it to collect more photons and speckles within a single exposure [5–8]. The camera's exposure time is usually longer than the decorrelation time of the speckle field, causing multiple evolving speckle patterns to accumulate in one frame. This results in a blurred image due to speckle pattern fluctuations.This blurring effect is primarily driven by the movement of blood cells. By analyzing the degree of image blur—typically through speckle contrast calculation—one can estimate the speckle field's decorrelation time. Building on this principle, compact and wearable systems have been developed to measure BF continuously and noninvasively through speckle contrast analysis.

There are two main methods used to calculate speckle contrast. The first employs a sliding window—commonly 7 × 7 pixels—across the image to compute local contrast. This method works well when the signal level is above the camera's noise threshold [9–14]. The second method analyzes the entire image, often containing over a million pixels, which is usually referred as speckle visibility spectroscopy (SVS) [15–18],and is more effective when the signal is weak or near the noise level.

This report introduces a novel and cost-effective system developed for the real-time monitoring of relative cerebral blood flow (CBF) within the deeper layers of the brain. The system is based on interferometric Speckle Visibility Spectroscopy (iSVS) integrated with a time-gating strategy, which facilitates the selective detection of photons that have penetrated to greater depths, thereby enhancing sensitivity to deep cerebral regions. By combining digital holography with temporal gating and incorporating interferometric enhancement, the approach yields a substantial improvement in the signal-to-noise ratio during speckle contrast analysis. The complete Speckle Contrast Optical Spectroscopy (SCOS) setup can be assembled at an approximate cost of €900, offering a compact and accessible platform for deep-brain CBF imaging applications.

The report is organized as follows. First, the theoretical background is presented, covering the principles of holography, time-gating, Laser Speckle Contrast Imaging (LSCI), and interferometric Speckle Visibility Spectroscopy (iSVS). Next, the design and experimental setup of the LSCI and iSVS systems are described, followed by an overview of the data processing methods used to extract flow information from the recorded camera images. Subsequently, a comparative experimental analysis is conducted to evaluate flow measurements obtained from both LSCI and iSVS across human-mimicking phantoms of varying thicknesses. Finally, the report concludes with a summary of the findings and a discussion of prospective directions for future *in vivo* experimentation.

2

Theory

This chapter presents the theoretical foundations underlying several advanced optical imaging modalities, with a particular focus on holography, time-gated imaging, Laser Speckle Contrast Imaging (LSCI), and Interferometric Speckle Visibility Spectroscopy (iSVS). For each technique, we outline the core physical principles, relevant mathematical formulations, and practical considerations essential for implementation. Together, these frameworks establish the conceptual basis for leveraging optical imaging in biomedical diagnostics and material characterization.

A unifying objective across these modalities is the noninvasive quantification of cerebral blood flow (CBF), a critical physiological parameter. A widely used metric in this context is the Blood Flow Index (BFI), derived from the first-order normalized electric field autocorrelation function, $g_1(\tau)$. This function characterizes the temporal decay in coherence arising from dynamic scattering, primarily due to the motion of red blood cells (RBCs) within biological tissue [19]. Each method for estimating $g_1(\tau)$ offers distinct advantages, while also introducing specific limitations that drive ongoing innovation.

The normalized first-order autocorrelation function $g_1(\tau)$ is defined as:

$$g_1(\tau) = \exp\left(-K^2\langle\Delta r^2(\tau)\rangle\right), \tag{2.1}$$

where K is the effective scattering wavevector, and $\langle\Delta r^2(\tau)\rangle$ is the mean square displacement (MSD) of RBCs over a time delay τ. This MSD accounts for both diffusive and convective motion components and is given by:

$$\langle\Delta r^2(\tau)\rangle = 6D\tau + v_{\mathsf{RBC}}^2\tau^2, \tag{2.2}$$

with D denoting the diffusion coefficient and v_{RBC} representing the convective velocity of red blood cells. The Blood Flow Index is then formulated as:

$$\mathsf{BFI} \propto \alpha \cdot \langle\Delta r^2(\tau)\rangle, \tag{2.3}$$

where α is a proportionality constant that reflects the fraction of dynamically scattered light. BFI serves as a robust quantitative indicator of microvascular perfusion and plays a pivotal role in methods such as Diffuse Correlation Spectroscopy (DCS), Laser Speckle Contrast Imaging (LSCI), and Interferometric Speckle Visibility Spectroscopy (iSVS).

2.1. Holography

Holography employs a coherent light source to capture and reconstruct the amplitude and phase information of a wavefront by utilizing the interference between an object wave and a reference wave. A

notable application of holography is coherence-gated imaging, which facilitates imaging through turbid media by employing light with a short coherence length.

In digital holography, the digital hologram is recorded in the Fourier plane, allowing the focused image to be reconstructed through a digital Fourier transform. Consequently, the reconstruction algorithm is a straightforward implementation of the Fast Fourier Transform (FFT), which offers faster numerical reconstruction compared to algorithms based on the Fresnel approximation [20]. Additionally, Fourier filtering techniques, including high-pass filtering, dark-field imaging, and phase-contrast imaging, can be conveniently applied to the digital hologram without the need for additional optical components.

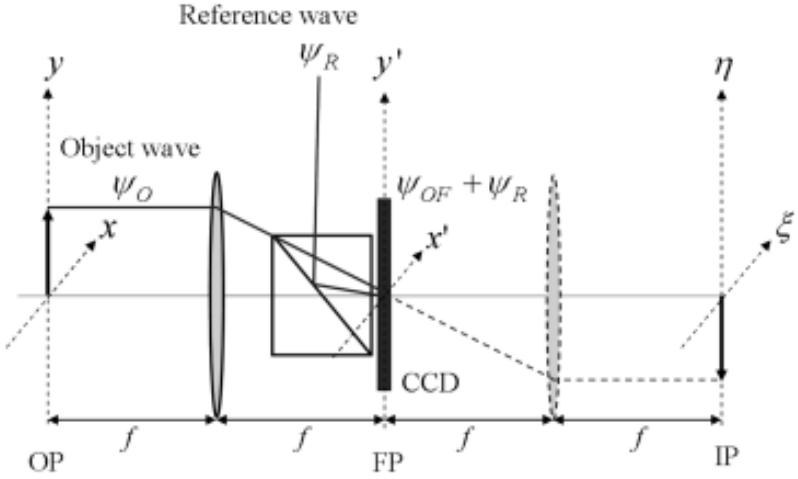

Figure 2.1: Optical setup for digital holography: OP (object plane), FP (Fourier plane), IP (image plane), ψ_O (object wave), ψ_{OF} (Fourier transform of the object wave), and ψ_R (reference wave). Lenses are positioned to perform the Fourier transformation [20]

The foundational setup for digital recording in digital holography is illustrated in figure 2.1. A coherent light source generates both a reference plane wave and an object wave. The object wave, denoted as $\psi_O(x, y)$, undergoes an optical Fourier transformation via a lens with a focal length f. For an ideal lens, the object wave at the Fourier plane is expressed as:

$$\psi_{OF}(x', y') = \frac{i}{\lambda f} \exp\left(-\frac{i4\pi f}{\lambda}\right) \int_{-\infty}^{+\infty} \int_{-\infty}^{+\infty} \psi_O(x, y) \exp\left(\frac{-i2\pi}{\lambda f}(xx' + yy')\right) dxdy, \tag{2.4}$$

where λ represents the wavelength of the source, and $\mathcal{F}$ denotes the Fourier transform.

The reference wave is given by:

$$\psi_R = \psi_{R_0} \exp\left(\frac{i2\pi}{\lambda}(v_{x_0}x + v_{y_0}y)\right), \tag{2.5}$$

where v_{x_0} and v_{y_0} are the spatial wavenumbers. When the object and reference waves are matched at the Fourier plane by adjusting the reference wave's path length, the intensity of the hologram is:

$$I_H(x', y') = |\psi_R|^2 + |\psi_{OF}|^2 + \psi_R^* \psi_{OF} + \psi_R \psi_{OF}^*, \tag{2.6}$$

where the first two terms represent the zero-order diffraction, and the latter terms correspond to the holographic and conjugate images.

Numerical reconstruction of the digital hologram is achieved using a Fourier transform, analogous to the optical Fourier transformation performed by a lens. The Fourier transform of the hologram intensity is expressed as:

$$\mathcal{F}[I_H] = \mathcal{F}[|\psi_R|^2] + \mathcal{F}[|\psi_{OF}|^2] + \mathcal{F}[\psi_R^* \psi_{OF}] + \mathcal{F}[\psi_R \psi_{OF}^*], \tag{2.7}$$

where the holographic image and its conjugate are spatially separated from the zero-order image. Consequently, numerical Fourier transformation provides both amplitude and phase information about the object.

2.2. Time-Gated Imaging

In highly scattering media such as biological tissue, photons undergo stochastic trajectories due to repeated scattering events. Photons that penetrate deeper into the tissue typically follow longer optical paths and, consequently, arrive at the detector with greater time delays relative to those scattered near the surface.

Time-gated detection leverages this time-of-flight behavior by selectively capturing photons within defined temporal windows. Photons arriving later are statistically more likely to have interacted with deeper tissue layers. By isolating these photons, time-gated systems enhance sensitivity to subsurface structures while attenuating the influence of superficial or multiply scattered light [21–24].

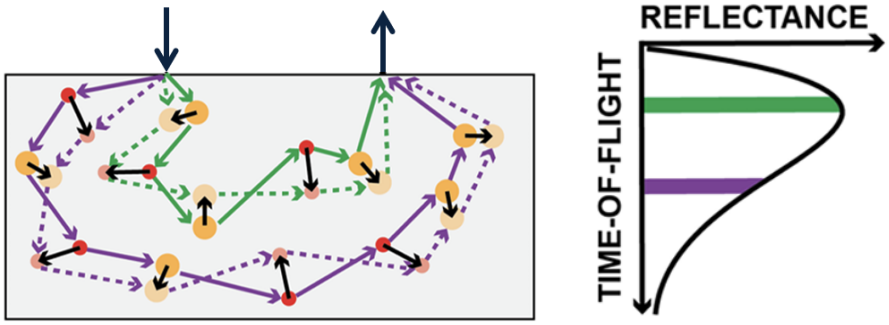

Figure 2.2: Schematic illustration of photon arrival time registration [24]

As shown in Figure 2.3, temporal resolution of photon arrival times allows the construction of histograms or time-gated detection windows. This approach enhances depth specificity by effectively excluding early-arriving photons that predominantly sample superficial regions. The resulting measurements offer high-contrast, depth-resolved flow information, which is particularly advantageous for studies of cerebral hemodynamics.

2.3. Laser Speckle Contrast Imaging (LSCI)

Laser Speckle Contrast Imaging (LSCI) relies on the coherent properties of laser light to generate speckle patterns when interacting with scattering media. These speckle patterns, which are sensitive to the dynamic motion of scatterers such as red blood cells (RBCs) in tissue vasculature, provide critical information about blood flow and hemodynamic parameters [25]. The patterns are formed due to the interference of scattered light waves that undergo constructive and destructive interference upon reflection or transmission through the tissue.

The resultant speckle intensity at any point is governed by the superposition of the electric field contributions from all scatterers in the illuminated region. Mathematically, the electric field A at the detector is expressed as:

$$A = \frac{1}{\sqrt{N}} \sum_{n=1}^{N} a_n e^{i\phi_n} \tag{2.8}$$

where a_n and ϕ_n represent the amplitude and phase of the n-th scattered wave, respectively, and N is the total number of scatterers contributing to the detected signal.

The intensity I, which determines the observed speckle pattern, is calculated as the square of the magnitude of the electric field:

$$I = |A|^2 \tag{2.9}$$

For fully developed speckles, the intensity follows a negative exponential probability distribution, while the amplitude follows Rayleigh statistics.

As shown in figure 2.3(a), red blood cells flowing inside blood vessels act as the main source of mobile scatterers in biological tissue. Speckles are formed on the camera's imaging plane by the diffraction of

scattered light through the camera aperture. This process is illustrated in figure 2.3(b).

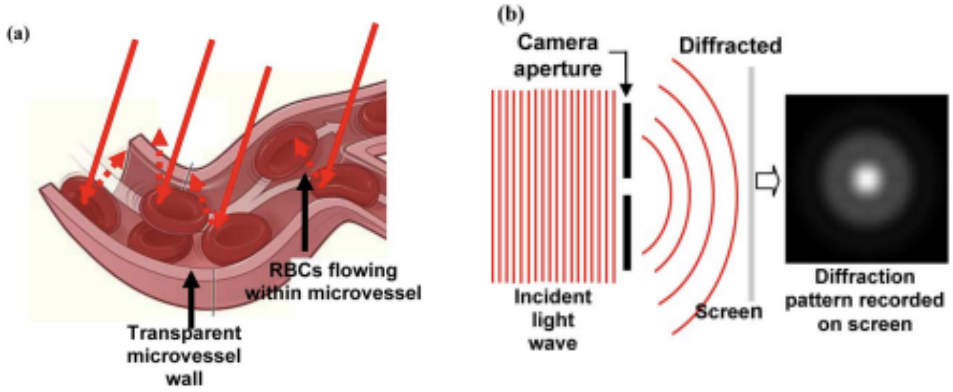

Figure 2.3: Production of laser speckles (a) Back-scattered laser light from blood cells flowing in the microvessels (b) The light waves thus scattered are diffracted through the camera aperture to form an interference pattern on the camera screen [6]

A key parameter in LSCI is the speckle contrast K, which measures the variation in speckle intensity. It is defined as:

$$K = \frac{\sigma}{\langle I \rangle} \tag{2.10}$$

where σ is the standard deviation of the intensity fluctuations and $\langle I \rangle$ is the mean intensity. This parameter reflects the dynamics of the scatterers: higher contrast corresponds to relatively static regions, while lower contrast indicates faster motion, such as blood flow.

The physical dimensions of the speckle, specifically the speckle size S, are determined by the wavelength λ of the laser light, the magnification M of the optical system, and the f-number $f\#$ of the imaging lens. The speckle size is given by [5]:

$$S = 2.44\lambda(1 + M)f\# \tag{2.11}$$

Optimal speckle size, typically twice the pixel size of the imaging detector, ensures accurate sampling and minimizes aliasing artifacts. The sensitivity of LSCI to scatterer motion makes it a powerful tool for assessing blood flow dynamics in biological tissues.

LSCI techniques rely on the measurement of speckle contrast to visualize blood flow dynamics. These techniques use the spatial variance of speckle intensity to assess the motion of scatterers, such as red blood cells (RBCs), within tissues. The relationship between the temporal decorrelation of speckles and the camera exposure time forms the foundation of this approach.

The spatial variance of time-averaged speckles, $\sigma_s^2(T)$, is directly related to the autocovariance of speckle intensity fluctuations, $C(\tau)$. The variance is expressed as an integral over the exposure time, T, as follows [5]:

$$\sigma_s^2(T) = \frac{1}{T}\int_0^T C(\tau)\, d\tau \tag{2.12}$$

where $C(\tau)$ is the autocovariance of the intensity signal over a time delay τ. This relationship captures the temporal dynamics of scatterer motion.

The autocovariance of the speckle intensity is mathematically defined as [5]:

$$C(\tau) = \langle I(t) - \langle I \rangle \rangle \cdot \langle I(t+\tau) - \langle I \rangle \rangle \tag{2.13}$$

where $I(t)$ is the intensity at a given time t, and $\langle I \rangle$ is the mean intensity. Under the assumption of exponential decay of speckle intensity fluctuations, the autocovariance simplifies to [5]:

$$C(\tau) = \langle I \rangle^2 \exp\left(-\frac{2\tau}{\tau_c}\right) \tag{2.14}$$

where τ_c is the correlation time of the speckles, inversely related to the velocity of the scatterers. Faster scatterer motion leads to shorter τ_c, while slower motion results in longer τ_c.

The local speckle contrast K_s, which is a measure of the spatial variations in speckle intensity, can be derived by combining the spatial variance and autocovariance. The contrast is given by [5]:

$$K_s = \frac{\sigma_s}{\langle I \rangle} = \sqrt{\frac{\tau_c}{2T}\left(1 - \exp\left(-\frac{2T}{\tau_c}\right)\right)} \tag{2.15}$$

For rapidly moving scatterers (small τ_c), the contrast decreases because the speckle decorrelation occurs within the exposure time.

Temporal speckle contrast K_t is another method for calculating contrast, focusing on variations in intensity over time for a specific pixel location. The temporal speckle contrast is defined as [25]:

$$K_t = \frac{\sigma_t}{\langle I \rangle_t} = \frac{\sqrt{\frac{1}{(N-1)}\sum_{n=1}^{N}\left(I(i,j,n) - \langle I(i,j)\rangle\right)^2}}{\langle I \rangle_{i,j}} \tag{2.16}$$

where N is the number of frames, $I(i,j,n)$ is the intensity at pixel (i,j) in the n-th frame, and $\langle I(i,j)\rangle$ is the mean intensity over all frames. Temporal contrast provides higher spatial resolution but at the cost of reduced temporal sensitivity.

The following relationship bewteen the velocities V of scatters and the decorrelation time τ is typically used as an approximation [6]:

$$V = \frac{\lambda}{2\pi\tau} \tag{2.17}$$

2.4. Interferometric Speckle Visibility Spectroscopy (iSVS)

Interferometric Speckle Visibility Spectroscopy (ISVS), also referred to as Speckle Contrast Optical Spectroscopy (SCOS), is a non-invasive optical technique primarily used for investigating dynamics within biological tissues and other scattering media. This method leverages the statistical properties of speckle patterns—random intensity distributions that arise from the interference of coherent light scattered by a sample [15–18].

ISVS is based on the principle of interferometry to enhance the detection and analysis of weak optical signals. Fundamentally, the technique combines a reference beam with a signal beam in an interferometric setup, as shown in figure 2.4(a), to extract detailed information about dynamic processes, such as blood flow, through speckle pattern analysis.

The ISVS configuration superimposes a weak signal beam E_S with a strong reference beam E_R. The total intensity recorded at a position $r = (x, y)$ in the observation plane is expressed as:

$$I(r,t) = |E_R|^2 + |E_S|^2 + 2\sqrt{|E_R|^2|E_S(r)|^2}\cos(k_0 x \sin\theta + \phi_S), \tag{2.18}$$

where k_0 is the free-space wave vector, θ is the tilt angle of the reference beam, and $\phi_S(r)$ is the phase difference between the reference and signal beams. The Fourier transform of $I(r,t)$, facilitated by off-axis holography, separates the DC components from the interference terms, enabling the reconstruction of the complex field $E_S(r)$.

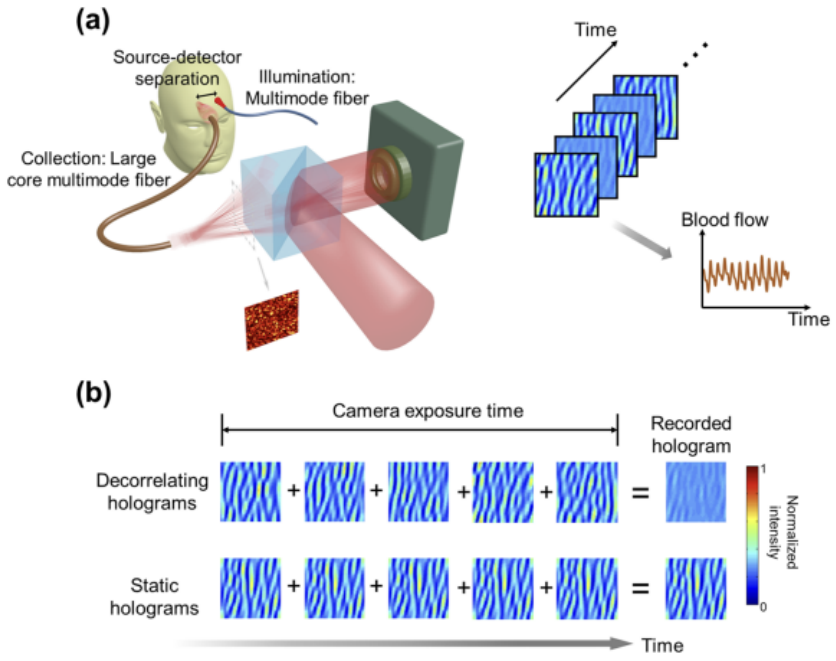

Figure 2.4: Principle of ISVS. (a) Schematic of the ISVS setup. (b) Difference between decorrelating and static diffused optical fields recorded in a single camera frame [16]

For the setup depicted in figure 2.4, the interference pattern recorded by the camera is:

$$I(r,t) = \int_0^T [|E_R|^2 + |E_S|^2 + 2\sqrt{|E_R|^2|E_S(r)|^2}\cos(k_0 x \sin\theta + \phi_S)]dt, \tag{2.19}$$

where $t = 0$ marks the beginning of the exposure, and T represents the exposure time. Due to the off-axis configuration, the third interference term in the integral occupies a distinct location in Fourier space, enabling its isolation for complex field reconstruction, as illustrated in figure 2.5.

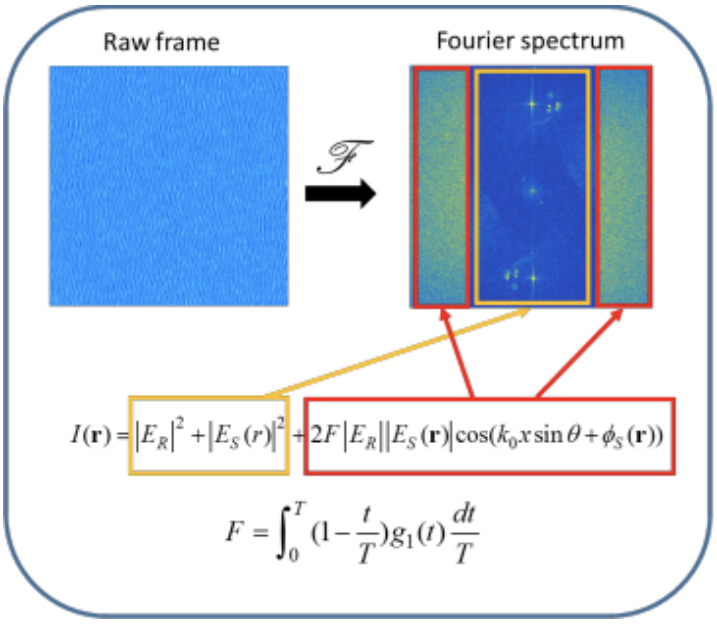

Figure 2.5: Fourier-transformed raw frame highlighting three lobes containing information about the reference and sample beams [16]

The interference signal can be defined as:

$$H(r) = \frac{1}{T}\int_0^T 2|E_R||E_S(r,t)|\cos\phi_S(r,t)\,dt. \tag{2.20}$$

Rewriting this, we get:

$$H(r) = \frac{1}{T}\int_0^T |E_R||E_S(r,t)|e^{i\phi_S(r,t)}\,dt + \frac{1}{T}\int_0^T |E_R||E_S(r,t)|e^{-i\phi_S(r,t)}\,dt. \tag{2.21}$$

The ISVS signal $S(r)$ is defined by isolating the first phase-conjugated pair:

$$S(r) = \frac{1}{T}\int_0^T |E_R||E_S(r,t)|\exp(i\phi_S(r,t))\,dt. \tag{2.22}$$

The second moment of $S(r)$ encapsulates the field decorrelation function $g_1(t)$:

$$\begin{aligned}\langle|S(r)|^2\rangle &= \frac{I_R}{T^2}\int_0^T\int_0^T dt_1 dt_2 E_S(r,t_1)\exp(i\phi_S(r,t_1))E_S(r,t_2)\exp(-i\phi_S(r,t_2)) \\ &= \frac{I_R\overline{I_S}}{T}\int_0^T 2\left(1-\frac{t}{T}\right)g_1(t)\,dt,\end{aligned} \tag{2.23}$$

where I_R and $\overline{I_S}$ denote the intensities of the reference and mean signal beams, respectively. These parameters can be calibrated prior to experimentation.

To quantify the visibility of interference fringes, the equivalent visibility factor is defined as:

$$F = \frac{\langle|S(r)|^2\rangle}{I_R\overline{I_S}} = \frac{1}{T}\int_0^T 2\left(1-\frac{t}{T}\right)g_1(t)\,dt. \tag{2.24}$$

The factor F directly depends on $g_1(t)$ and the camera exposure time T. For static samples, $F = 1$, indicating high fringe contrast. In rapidly decorrelating fields, $F = 2\tau/T$, reflecting diminished fringe visibility.

3

Methods

Broad-area laser diodes (BALDs) were chosen for this study largely because they strike an appealing balance between performance and practicality. Their standout traits—namely high optical output, relatively short coherence length, and cost efficiency—make them particularly well-suited for applications like time-gated imaging and dynamic scattering analysis in biological tissues. A key advantage lies in their expansive lateral emission aperture, often over 100 μm, which allows these diodes to handle substantial current densities across a wide active region. As a result, they can deliver continuous-wave (CW) power outputs in the multi-watt range, all without requiring intricate cooling systems or the stabilization that external cavities typically demand [26].

Another strength of BALDs is their inherently multimode spatial emission and broad spectral output, both of which contribute to their characteristically short coherence lengths. This feature proves especially useful in coherent imaging setups, as it helps suppress speckle noise and curtails multipath interference [27]. Consequently, a time-gating strategy becomes more viable due to the low coherence length, which effectively enhances depth discrimination.

On top of these merits, BALDs are relatively inexpensive, especially when stacked against alternatives like superluminescent diodes or pulsed solid-state lasers. Their straightforward monolithic architecture, ease of mass production, and compact packaging make them a convenient and scalable option for both biomedical and industrial optical systems [28]. Altogether, these factors made BALDs the obvious choice for our illumination needs—offering a smart mix of power, simplicity, and affordability.

This chapter outlines the experimental methodology employed to investigate optical flow imaging using two distinct configurations: on-axis and off-axis. Both modalities were implemented using a custom-designed system centered around broad-area laser diodes (BALDs), chosen for their high optical output, short coherence length, and cost-effectiveness—features that collectively enable time-gated imaging and coherent detection in scattering media.

In the sections that follow, we detail the theoretical principles and optical arrangements underlying each imaging approach. We describe the construction of the interferometric setups, the calibration and imaging protocols, and the computational pipelines used to extract quantitative flow metrics. Together, these methods form a comprehensive platform for evaluating speckle dynamics and reconstructing flow patterns in tissue-mimicking environments.

3.1. Coherence Length Experiment

3.1.1. Principle

To experimentally validate the coherence length of the low-coherence light sources, a Michelson interferometer was constructed. Interferogram intensity was recorded using a photodetector (PD). The reference arm of the interferometer was mounted on a motorized linear translation stage, enabling precise control of the optical path difference between the reference and sample arms. As the reference arm was scanned, the PD measured the interference signal as a function of path length difference. Due

to the finite coherence of the light source, the recorded signal exhibited a fringe envelope.

The full width at half maximum (FWHM) of the interference envelope was determined by fitting the recorded intensity profile against the displacement of the reference mirror. The lateral coherence length, L_c, was then estimated as:

$$L_c = \text{FWHM}$$

which characterizes the path length over which the light retains sufficient phase coherence to produce interference.

3.1.2. Methodology

In this experiment, three low-coherence laser diodes were evaluated: the Thorlabs L808P200, L808P500, and 785P400K70.A04. The interference signal was captured using a photodetector (Thorlabs APD130A2), which recorded the intensity profile as the optical path length was systematically varied. A schematic of the experimental setup is provided in Figure 3.1.

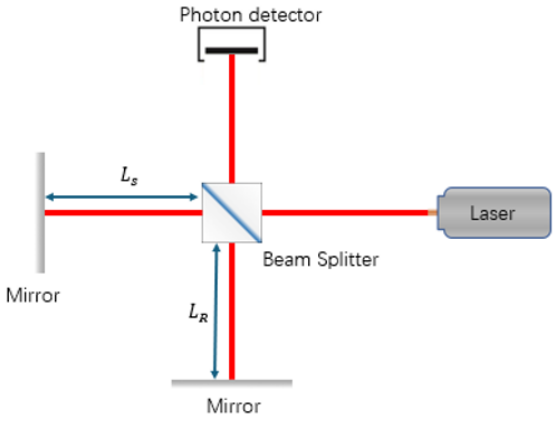

Figure 3.1: Schematic of the coherence length experimental setup

The mirror in the reference arm was mounted on a motorized linear translation stage, which moved at a constant velocity of 0.47 cm/s, generating a controlled variation in path length. As the mirror translated, the interference fringes observed by the photodetector formed an envelope pattern that reflected the coherence characteristics of each light source. The full width at half maximum (FWHM) of these fringe envelopes was measured to estimate the coherence length of each laser diode.

Experimental results for each diode are shown in figures 3.2, 3.3, and 3.4.

(a) **(b)**

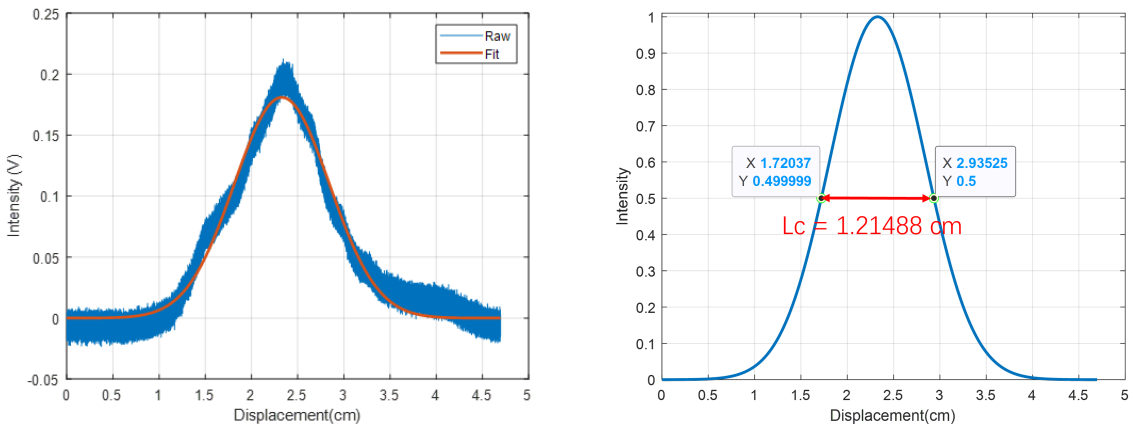

Figure 3.2: Coherence length results for Thorlabs L808P200 (a) Raw signal and fitted envelope (b) FWHM estimation ($L_c = 1.21488$ cm)

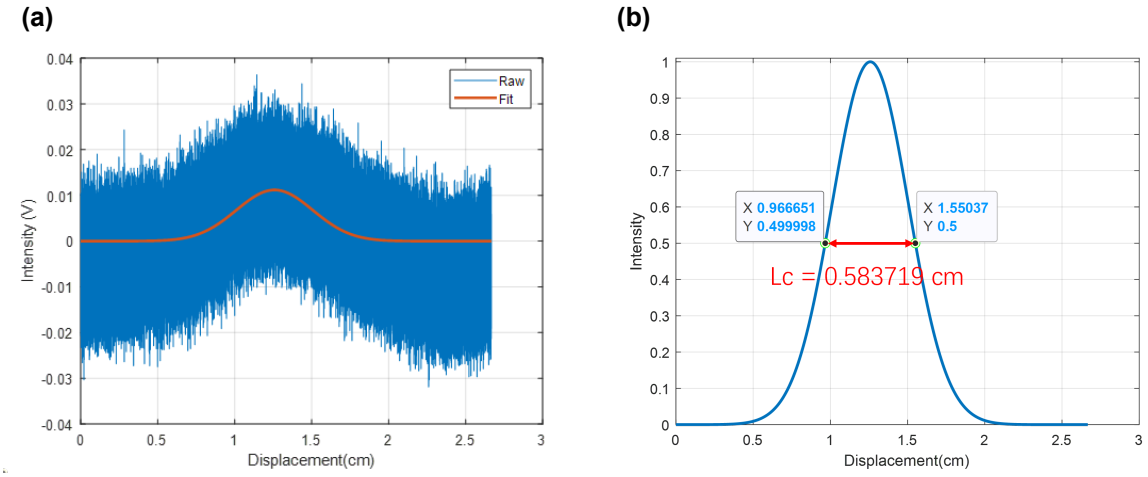

Figure 3.3: Coherence length results for Thorlabs L808P500 (a) Raw signal and fitted envelope (b) FWHM estimation ($L_c = 0.583719$ cm)

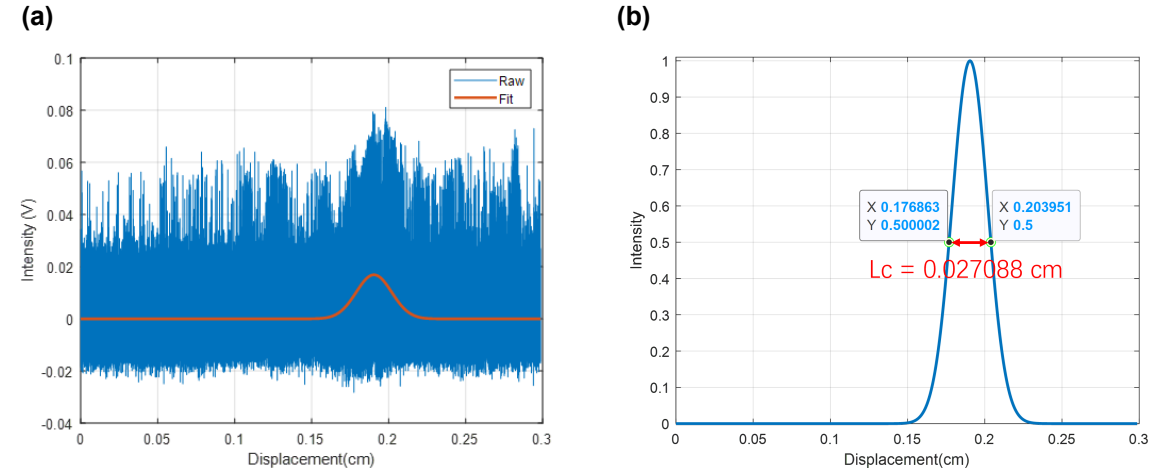

Figure 3.4: Coherence length results for Thorlabs 785P400K70.A04 (a) Raw signal and fitted envelope (b) FWHM estimation ($L_c = 0.027088$ cm)

Based on the measured coherence properties and practical system requirements, the Thorlabs L808P200 laser diode—exhibiting a coherence length of approximately 1.2 cm—was selected as the primary illumination source for the subsequent experiments. The overall system was designed and operated in compliance with internationally recognized laser safety standards, including ANSI Z136.1 and IEC 60825-1. Beyond fulfilling safety protocols, this diode offers several practical benefits: it is cost-effective, supports straightforward electronic control, and provides operational ease. These attributes collectively make it a highly suitable candidate for seamless integration into the experimental platform.

3.2. Tissue-mimicking Phantoms

To replicate the optical properties of layered human tissue, tissue-mimicking phantoms were fabricated using a combination of scattering and absorbing agents embedded in a silicone-based matrix. The base material, polydimethylsiloxane (PDMS), was selected due to its mechanical stability, optical transparency in the near-infrared spectrum, and excellent biocompatibility. Titanium dioxide (TiO_2) powder was incorporated as the primary scattering agent, while carbon black powder (CBP) was added to introduce absorption—effectively simulating the light attenuation characteristics of biological tissues such as skin and skull [29].

To prepare the final phantom mixture, specific volumes of each stock were diluted into pure PDMS to achieve the desired concentrations. The curing agent—comprising methylhydrogenated silica, dimethylvinylated silica, and trimethylated silica—was then added at 10% w/w relative to the total PDMS mixture.

This final blend was subjected to blade mixing for 30 minutes, followed by 1 hour of gentle rocking to reduce sedimentation during curing. To eliminate entrapped air, the mixture was degassed in a vacuum desiccator for over 2 hours before being carefully poured into 87.0 mm diameter Petri dishes (Nunc, Thermo Fisher).

Initial curing was carried out at room temperature for approximately 12 hours on a leveled surface to ensure uniform solidification and to prevent phase separation of the dispersed particles. Subsequently, the samples were transferred to a 75°C oven and baked for over 6 hours to complete the curing process. The final cured phantoms were easily demolded and exhibited no visible sedimentation or aggregation. Reflectance measurements confirmed optical homogeneity across the sample thickness.

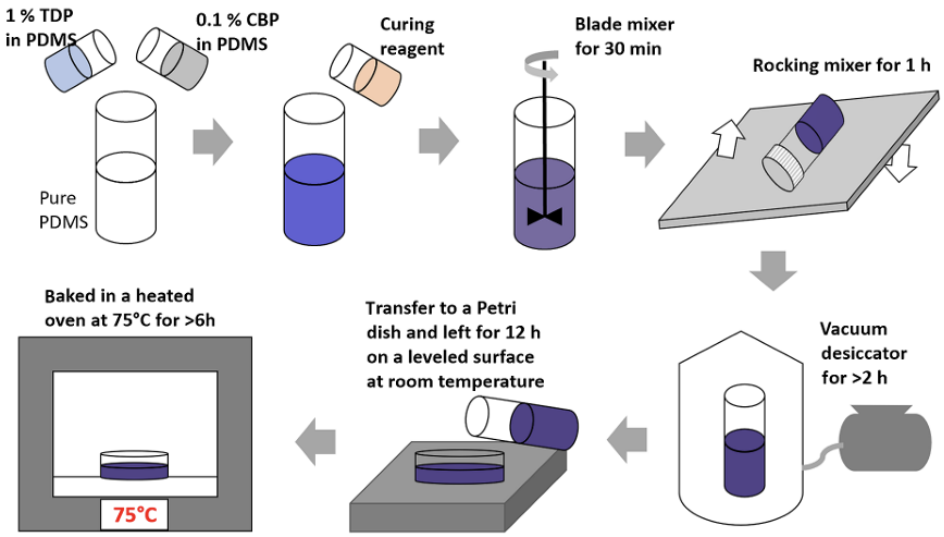

Figure 3.5: Step-by-step phantom fabrication procedure

A trace quantity of CBP (0.0055 wt%) was included to replicate the absorption of the scalp, which has a reported absorption coefficient of 0.3–0.5 mm^{-1} at 800 nm [30]. Meanwhile, 0.1% titanium dioxide powder (TDP) was added to introduce scattering similar to that of bone tissue, whose reduced scattering coefficient at 800 nm ranges from 8.2 to 19.8 mm^{-1} [31]. This formulation enabled the phantom to emulate both the absorption and scattering characteristics of layered biological structures.

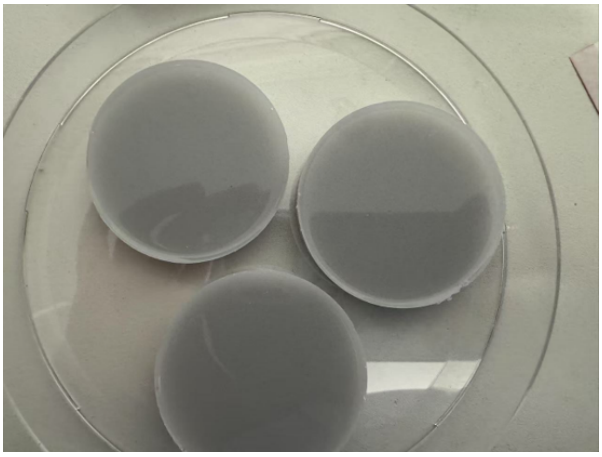

Figure 3.6: Photograph of cured PDMS phantoms

3.3. On-axis Configuration

The on-axis configuration used in this study is based on Laser Speckle Contrast Imaging (LSCI), augmented by a coherence-based ToF gate. A low-cost multimode laser diode is employed to establish the coherence gate. By tuning the optical path length difference (OPD) between the sample and reference arms, we selectively interfere photons with specific ToFs. This enables operation at short SD separations, thereby improving spatial resolution and photon throughput while maintaining sensitivity to deep flow. The resulting system offers a cost-effective and practical solution for high-resolution, depth-sensitive cerebral blood flow (CBF) monitoring.

3.3.1. Principle

The instantaneous optical intensity recorded by the camera over an exposure time T at pixel p is given by:

$$I_{\mathrm{p}}(s,t) = \int_0^T \left\{ |E^{\mathrm{p}}_{\mathrm{LO}}(t)|^2 + |E^{\mathrm{p}}_{\mathrm{sam}}(t)|^2 + 2|E^{\mathrm{p}}_{\mathrm{LO}}(t)||E^{\mathrm{p}}_{\mathrm{sam}}(s,t)| \cos[k_0 x \sin\theta + \varphi^{\mathrm{p}}_s(t)] \right\} dt \tag{3.1}$$

Here, $E^{\mathrm{p}}_{\mathrm{LO}}(t)$ and $E^{\mathrm{p}}_{\mathrm{sam}}(s,t)$ denote the electric fields of the local oscillator (reference arm) and the sample arm (with scattering path length s) at pixel p, respectively. The terms $k_0 x \sin\theta$ and $\varphi^{\mathrm{p}}_s(t)$ represent the spatial carrier phase and the time-varying phase induced by dynamic scattering. The optical path difference (OPD)—and thus the probed path length s—can be adjusted by translating the mirror in the reference arm.

In this configuration, no spatial filtering is applied to remove the DC components. Therefore, the raw intensity image captured by the camera includes both static background and fluctuating interference terms.

The speckle contrast K is computed across a spatial window as the normalized standard deviation of the recorded intensity:

$$K = \frac{\sigma(I_{\mathrm{p}}(s,t))}{\langle I_{\mathrm{p}}(s,t) \rangle} \tag{3.2}$$

Assuming that the sample intensity $I_{\mathrm{sam}}(s,t) = |E^{\mathrm{p}}_{\mathrm{sam}}(s,t)|^2$ is approximately stationary over the exposure time T, and that the phase $\varphi^{\mathrm{p}}_s(t)$ follows a zero-mean Gaussian random process, the intensity fluctuations are dominated by the interference term. The autocorrelation of the cosine modulation yields:

$$\langle \cos[\varphi^{\mathrm{p}}_s(t_1)] \cos[\varphi^{\mathrm{p}}_s(t_2)] \rangle = \frac{1}{2} \Re[g_1(t_1 - t_2)] \tag{3.3}$$

Accordingly, the variance of the intensity is:

$$\sigma^2(I_{\mathrm{p}}) = \frac{2 I_{\mathrm{LO}} \cdot \overline{I_{\mathrm{sam}}(s)}}{T^2} \int_0^T \int_0^T \frac{1}{2} \Re[g_1(t_1 - t_2)] dt_1 dt_2 \tag{3.4}$$

Using the standard convolution identity:

$$\int_0^T \int_0^T \Re[g_1(t_1 - t_2)] dt_1 dt_2 = 2 \int_0^T \left(1 - \frac{t}{T}\right) \Re[g_1(t)] dt \tag{3.5}$$

we derive the speckle contrast squared as:

$$K^2 = \frac{4 I_{\mathrm{LO}} \cdot \overline{I_{\mathrm{sam}}(s)}}{(I_{\mathrm{LO}} + \overline{I_{\mathrm{sam}}(s)})^2} \cdot \int_0^T \frac{1}{T} \left(1 - \frac{t}{T}\right) \Re[g_1(t)] dt \tag{3.6}$$

This expression shows that K^2 depends on both the temporal field autocorrelation function $g_1(t)$ and the intensity ratio between the reference and sample arms. The contrast is maximized when $I_{\mathrm{LO}} = \overline{I_{\mathrm{sam}}(s)}$, corresponding to optimal interferometric visibility.

The first computational step involves determining the raw squared speckle contrast, K^2_{raw}, from the recorded image data. This measurement, however, inherently includes contributions from noise, leading to an inflated variance estimate. To address this, the adjusted squared speckle contrast, K^2_{adjusted}, is computed using [18]:

$$K^2_{\text{adjusted}} = K^2_{\text{raw}} - K^2_{\text{shot}} - K^2_{\text{quant}} - K^2_{\text{cam}}, \tag{3.7}$$

where:

- K^2_{shot} compensates for shot noise,
- K^2_{quant} accounts for quantization noise, and
- K^2_{cam} corrects for the camera's readout and electronic noise.

Each of these components is computed for a given image I as:

$$K^2_{\text{shot}}(I) = \left(\frac{\gamma}{\mu(I)}\right) \tag{3.8}$$

$$K^2_{\text{quant}}(I) = \left(\frac{1}{12\mu(I)^2}\right) \tag{3.9}$$

$$K^2_{\text{cam}}(I) = \left(\frac{\sigma^2_{\text{cam}}}{\mu(I)^2}\right) \tag{3.10}$$

where γ is the analog-to-digital conversion gain factor, determined by the camera's gain and conversion factor (CF), i.e., $\gamma = \frac{\text{gain}}{\text{CF}}$.

In our experiments, gain was set in the range of 1 to 63 (equivalent to 0–18 dB) and tuned according to the signal intensity. For an camera with CF = 5.13 , the gain was selected to ensure the grayscale values remained between 40 and 255, minimizing quantization artifacts. The camera noise σ^2_{cam} was estimated by analyzing a set of 500 frames acquired in complete darkness.

Once K^2_{adjusted} is obtained, the blood flow index (BFI) can be computed as:

$$\text{BFI} = \frac{1}{K^2_{\text{adjusted}}} \tag{3.11}$$

3.3.2. Experimental arrangement

The experimental setup is based on a Laser Speckle Contrast Imaging (LSCI) system configured as a Michelson interferometer, as illustrated in Figure figure 3.7. A continuous-wave (CW) multi-mode 808 nm laser diode (L808P200, Thorlabs), thermally stabilized and capable of delivering up to 200 mW of optical power, serves as the illumination source. The high power output improves the speckle signal-to-noise ratio, particularly for deep-tissue imaging applications.

The laser beam is directed toward a 50:50 (R:T) non-polarizing beam splitter (BS011, Thorlabs), which divides the beam into a sample arm and a reference arm. In the sample arm, the beam illuminates a tissue-mimicking phantom. Backscattered light from the phantom is collected and directed onto a CMOS camera (DMK42AUC03, IMAGINGSOURCE), operated at a frame rate of 25 frames per second (fps) with an exposure time of 1/106 ms. This camera offers sufficient temporal resolution for speckle fluctuation analysis while maintaining a cost-effective design.

The phantom is backed by a fluid chamber, where a programmable pump is used to regulate the flow rate. This setup mimics dynamic scattering conditions, such as those caused by blood perfusion, and produces measurable temporal speckle fluctuations.

In the reference arm, a planar mirror is mounted on a motorized linear translation stage to precisely control the optical path length difference between the two arms, enabling stable interference. A neutral density (ND) filter (Thorlabs NDL-25C-2) is inserted into the reference arm to attenuate the beam intensity, ensuring balance between the sample and reference arms. This intensity matching enhances visibility and improves sensitivity in speckle-based measurements.

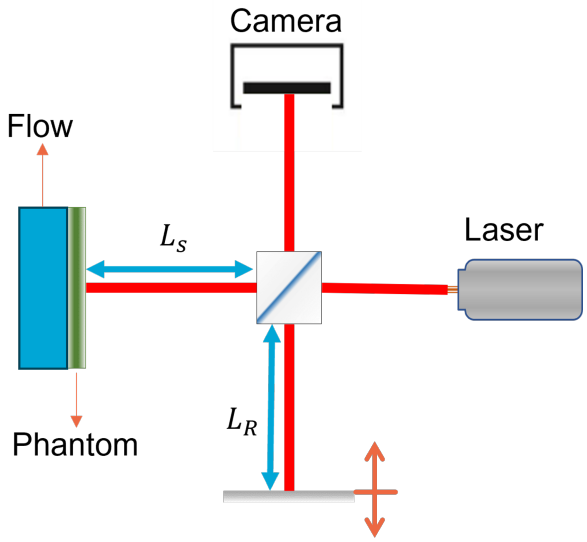

Figure 3.7: Schematic of the on-axis setup

The processing pipeline begins with the acquisition and storage of raw images captured by the camera during the experiment. These time-resolved frames contain temporal speckle fluctuations caused by dynamic light scattering within the sample. From this image sequence, the raw speckle contrast is calculated by evaluating the ratio of the standard deviation to the mean intensity across a defined temporal window for each pixel.

The resulting speckle contrast map is then calibrated to remove system-related noise and static background contributions, ensuring an accurate representation of flow dynamics. Once calibrated, the speckle contrast values are used to calculate the Blood Flow Index (BFI), which provides a quantitative measure of perfusion in the tissue sample. The processing pipeline for BFI estimation is illustrated in figure 3.8.

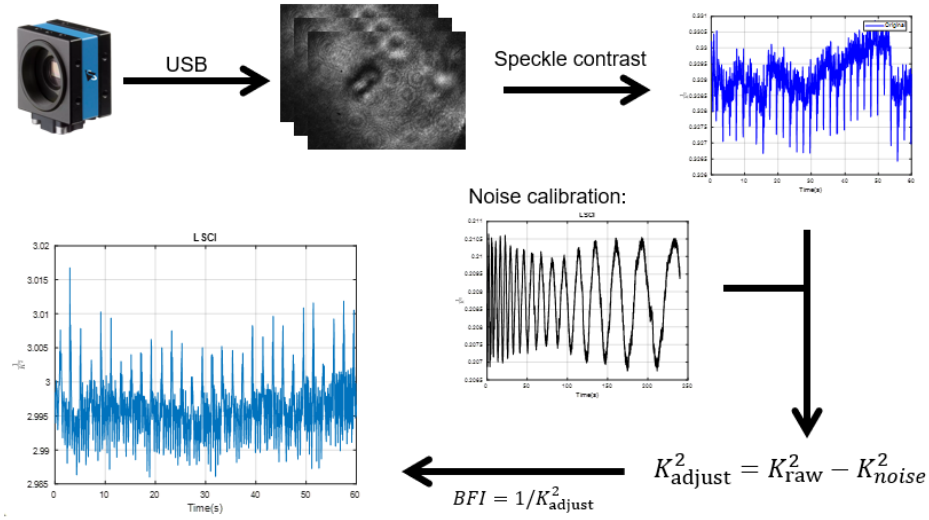

Figure 3.8: LSCI Processing analysis flowchart for deriving the blood flow from recorded camera images

3.4. Off-axis Configuration

The off-axis configuration employed in this study is primarily based on Interferometric Speckle Visibility Spectroscopy (ISVS), integrated with a coherence-based ToF gate. A low-cost multimode laser diode is

employed to establish the coherence gate. By tuning the optical path length difference (OPD) between the sample and reference arms, we selectively interfere photons with specific ToFs. This enables operation at short SD separations, thereby improving spatial resolution and photon throughput while maintaining sensitivity to deep flow. The resulting system offers a cost-effective and practical solution for high-resolution, depth-sensitive cerebral blood flow (CBF) monitoring.

3.4.1. Principle

The CG-iSVS works in an off-axis holography configuration, where the direct current (DC) component can be removed easily in spatial-frequency domain. The attenuated LO inteferes with the speckle pattern collimated from sample and the intensity at the pixel p is given by:

$$I_{\mathrm{p}}(s,t) = \int_0^T \{|E_{\mathrm{LO}}^{\mathrm{p}}(t)|^2 + |E_{\mathrm{sam}}^{\mathrm{p}}(t)|^2 + 2|E_{\mathrm{LO}}^{\mathrm{p}}(t)||E_{\mathrm{sam}}^{\mathrm{p}}(s,t)|\cos[k_0 x\sin\theta + \varphi_{\mathrm{s}}^{\mathrm{p}}(t)]\}dt$$

where T is the exposure time of camera, $E_{\mathrm{LO}}^{\mathrm{p}}(t)$ denotes the electric filed of the LO at pixel p, $E_{\mathrm{sam}}^{\mathrm{p}}(t)$ denotes the electric filed of the sample with scattering path length s at pixel p, $k_0 x\sin\theta$ and $\varphi_{\mathrm{s}}^{\mathrm{p}}(t)$ is the spatial and temporal phase different between them respectively. By adjusting the position of the retroreflector, the scattering path s can be adjusted. After the spatial Fourier transform, the DC component can be filtered out, take the positive band and nomalnized by the exposure time T, and assuming that the LO has a uniform distribution on the camera (i.e. $E_{\mathrm{LO}}^{\mathrm{p}}(t) = E_{\mathrm{LO}}(t)$):

$$S_{\mathrm{ac}}^{\mathrm{p}}(s,t) = \frac{1}{T}\int_0^T |E_{\mathrm{LO}}(t)||E_{\mathrm{sam}}^{\mathrm{p}}(s,t)|\exp[\varphi_{\mathrm{s}}^{\mathrm{p}}(t)]dt \tag{3.12}$$

The second moment of $S_{\mathrm{ac}}^{\mathrm{p}}(s,t)$ is given by:

$$< |S_{\mathrm{ac}}^{\mathrm{p}}(s,t)|^2 >= \frac{I_{\mathrm{LO}}\overline{I_{\mathrm{sam}}(s)}}{T}\int_0^T 2(1-\frac{t}{T})g_1(s,t)dt \tag{3.13}$$

where $I_{\mathrm{LO}} = |E_{\mathrm{LO}}(t)|^2$, $I_{\mathrm{sam}}(s) = |E_{\mathrm{sam}}(s,t)|^2$ and $g_1(s,t)$ is the field autocorrelation function of photons with scattering path s. After calibrating the I_{LO} and $\overline{I_{\mathrm{sam}}}$, the path-dependent visibility factor is given by:

$$F(s) = \frac{< |S_{\mathrm{ac}}^{\mathrm{p}}(s,t)|^2 >}{I_{\mathrm{LO}}\overline{I_{\mathrm{sam}}}} = \frac{\alpha(s)}{T}\int_0^T 2(1-\frac{t}{T})g_1(s,t)dt \tag{3.14}$$

Where I_{LO} and $\overline{I_{\mathrm{sam}}}$ can be measured by blocking the measurement arm and the reference arm respectively. $\overline{I_{\mathrm{sam}}(s)} = \alpha(s)\overline{I_{\mathrm{sam}}}$, where $\alpha(s)$ is the ratio between photons with sacttering path s and whole scattering photons. Compared with normal iSVS, the coherence gate produced by the multimode laser enable us to directly measure the path-dependent dynamics here.

The equations above do not account for system noise, which must be corrected to accurately obtain the theoretical visibility factor. The system noise originates from both the laser (shot noise, σ_{s}) and the camera. Camera noise primarily includes dark current, readout noise (σ_{r}), and quantization noise (σ_{q}) from digital conversion. Since the dark count varies across pixels, it introduces fixed pattern noise (FPN) [32]. In contrast, the readout and quantization noises are zero-mean and can be effectively suppressed by averaging multiple dark frames and subtracting the result from the raw image, thereby removing the FPN component.

Shot noise, readout noise, and quantization noise can be modeled as white noise, and are assumed to be uniformly distributed in the spatial frequency domain. Under this assumption, the measured visibility factor can be expressed as:

$$F'(s) = F(s) + \frac{(\sigma_{\mathrm{s}}^2 + \sigma_{\mathrm{r}}^2 + \sigma_{\mathrm{q}}^2)}{I_{\mathrm{LO}}\overline{I_{\mathrm{sam}}}} = F(s) + \frac{(\sigma_{\mathrm{s}}^2 + \sigma_{\mathrm{cam}}^2)}{I_{\mathrm{LO}}\overline{I_{\mathrm{sam}}}}$$

The individual noise terms are given by: $\sigma_{\mathrm{s}}^2 = \frac{\mathrm{G}\times\langle \mathrm{I}\rangle}{\mathrm{CF}}$ (G is the gain of camera, $\langle I\rangle$ is the average intensity accounts for the reference and the sample, and CF = full well capacity / $2^{\text{bit depth}}$), $\sigma_{\mathrm{q}}^2 = \frac{1}{12}$ [33], and σ_{r}^2, which can be estimated from the variance of dark frames (readout noise). By increasing the power of the reference beam such that $\sigma_{\mathrm{s}}^2 \gg \sigma_{\mathrm{cam}}^2$, the system approaches the shot-noise-limited SNR regime, and the visibility factor simplifies to:

$$F'(s) = F(s) + \frac{\sigma_{\mathrm{s}}^2}{I_{\mathrm{LO}}\overline{I_{\mathrm{sam}}}} \tag{3.15}$$

3.4.2. Experimental arrangement

The off-axis experimental configuration is a modified version of the on-axis system, designed to enable digital holography via spatially resolved interference, as shown in figure 3.9. A continuous-wave (CW) multi-mode laser diode operating at 808 nm (Thorlabs L808P200) is used as the illumination source. The laser beam is directed toward a 50:50 (Reflectivity:Transmission) non-polarizing beam splitter (Thorlabs BS008), which splits the beam into two optical paths: the sample arm and the reference arm.

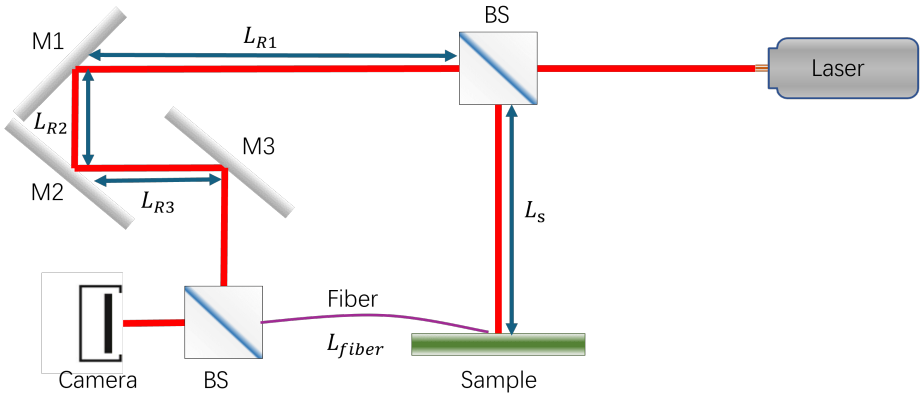

Figure 3.9: Schematic of the off-axis setup

In the sample arm, the beam illuminates a tissue-mimicking phantom. A multimode optical fiber with a 1000 µm core diameter (Thorlabs FP1000ERT) is positioned at a source–detector (S–D) separation of 2 mm from the illumination point to collect diffusely scattered light that has traversed the phantom and underlying flow medium. The collected light is then imaged onto a CMOS camera (IMAGINGSOURCE DMK42AUC03), operated at 25 frames per second with an exposure time of 1/106 ms. This configuration ensures a practical balance between speckle contrast sensitivity and system cost, while delivering adequate temporal resolution for speckle fluctuation analysis.

To simulate dynamic scattering conditions—such as those induced by blood flow—a programmable pump regulates the fluid flow in a chamber located behind the phantom. This design enables controlled and repeatable modulation of speckle patterns.

In the reference arm, traditional planar mirrors (M1 and M2) are replaced with broadband retroreflectors (Newport UBBR2.5-1S) to enhance alignment stability and precision in beam redirection. The retroreflectors is mounted on a motorized linear translation stage, allowing adjustments to the optical path length, which is essential for phase matching in interferometric measurements. A neutral density (ND) filter (Thorlabs NDL-25C-2) is placed in the reference arm to attenuate the beam intensity,

thereby balancing it with that of the sample arm. This power matching improves visibility and enhances sensitivity.

The beams from both arms recombine at the second beam splitter (Thorlabs BS011) and interfere to form a spatially modulated speckle pattern, which is recorded by the camera. The slight angular offset introduced between the reference and sample beams produces a spatial carrier frequency, enabling Fourier-domain separation and single-shot digital holographic reconstruction.

The signal processing pipeline is illustrated in Figure 3.10. Initially, a sequence of time-resolved speckle interference images is recorded. The reference intensity is subtracted from each frame to isolate dynamic scattering fluctuations. A spatial Fourier transform is then applied to each calibrated frame, and the high-frequency interference lobe—encoding flow-related signal—is extracted. Temporal integration of this lobe produces a time series representing the evolution of speckle fluctuations. A subsequent temporal Fourier transform of this signal reveals the dominant frequency component corresponding to flow rate, while the peak amplitude determines the signal-to-noise ratio (SNR), indicating the quality and reliability of the reconstructed blood flow signal.

As a comparison method, the LSCI approach illustrated in section 3.3 will be applied during data processing.

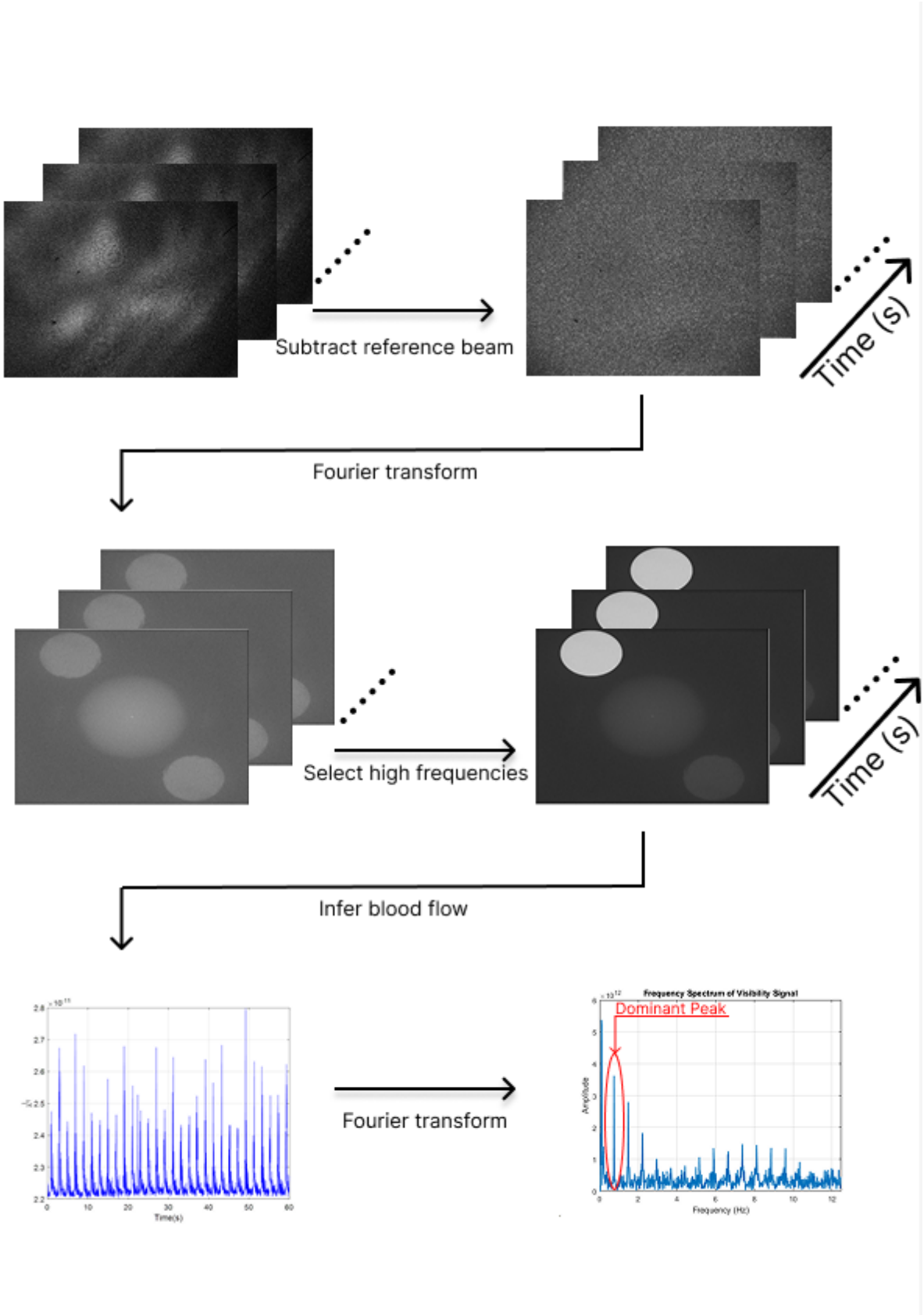

Figure 3.10: iSVS processing pipeline

4

Results

The peaks observed in the Fast Fourier Transform (FFT) visibility spectrum, such as the one shown in figure. 4.1, serve as quantitative indicators of the reconstruction quality of flow dynamics. In particular, the frequency component $\text{freq}_{\text{flow}}$ corresponds to the fundamental frequency of the pump-driven flow, while the associated spectral amplitude I_{flow} reflects the strength and clarity of the reconstructed signal. Compared to time-domain measurements—such as raw intensity fluctuations $I_S(t)$ or speckle contrast evolution—the frequency-domain representation offers improved sensitivity and specificity in evaluating signal fidelity.

To quantify signal quality, the signal-to-noise ratio (SNR) is computed in the frequency domain as:

$$\text{SNR} = \frac{I_{\text{flow}}}{\mu_{\text{noise}}}, \tag{4.1}$$

where I_{flow} denotes the amplitude of the visibility spectrum at the dominant flow frequency (i.e., $\text{freq}_{\text{HR}} = 0.5$ Hz), and μ_{noise} is the mean value of the spectral noise floor. The noise level is typically estimated from a high-frequency band (e.g., 10–12.5 Hz), where no physiological or system-induced signals are expected.

As shown in figure. 4.1, the reconstructed spectrum exhibits a clear peak at 0.5 Hz with a corresponding amplitude of 0.0686, consistent with the known pump cycle of 2 s per pulse. The noise region beyond 10 Hz shows only low-amplitude fluctuations, supporting the validity of this band for noise estimation. This frequency-domain SNR metric provides a robust and reproducible means of comparing flow signal quality across different acquisition conditions and configurations.

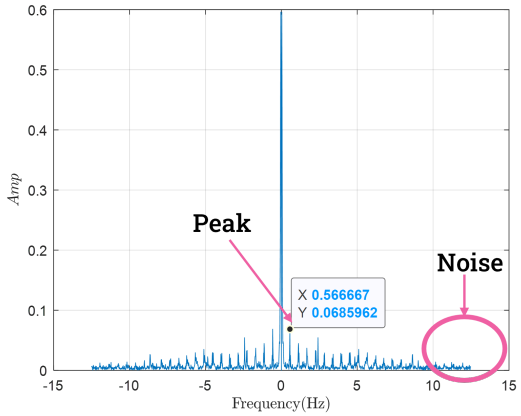

Figure 4.1: FFT visibility spectrum of the reconstructed flow signal.

In the coherence-based ToF-gated system, the optical path length difference D is defined as:

$$D = L_R - L_S, \tag{4.2}$$

where L_R and L_S denote the path lengths of the reference and sample arms, respectively. By carefully adjusting D—typically by translating a retroreflector in the reference arm—we can isolate interference from photons with specific ToF values, effectively gating them by depth.

With the spectral characteristics of the flow signal established, we now turn to a comparative assessment of two system configurations: on-axis and off-axis. To ensure fairness, both were tested under identical conditions—same illumination levels, same tissue-mimicking phantoms (1–2 cm thick), and matched acquisition parameters.

The following sections detail the comparative performance. Easy to comparasion all the results of BFi have been normalized between 0 and 1.

4.1. On-axis Configuration

To characterize dynamic scattering under the on-axis interferometric configuration, we analyzed speckle contrast fluctuations acquired at various path length differences between the sample and reference arms, using tissue-mimicking phantoms of different thicknesses, as illustrated in figure. 3.7. The objective was to identify the optimal path length condition for coherence gating—specifically, the condition that maximizes the signal-to-noise ratio (SNR) and enhances sensitivity to the deepest scattering layers within the coherence envelope of the illumination source.

Under the matched arm condition ($D = 0$ cm) and using a 1 cm thick phantom, time-resolved speckle contrast signals were recorded over a 60-second interval. As shown in figure. 4.2(a), the raw speckle signal (blue) displays periodic oscillations corresponding to the pump-driven flow. A moving average filter (red) overlays the data, delineating the envelope of contrast fluctuations induced by dynamic scattering.

To analyze the temporal characteristics of the signal, a Fast Fourier Transform (FFT) was applied to the time series. The resulting magnitude spectrum, shown in figure. 4.2(b), reveals a dominant frequency peak at approximately 0.5 Hz with a SNR of 4.44 dB, consistent with the 2 second pumping cycle thereby confirming the system's capacity to resolve low-frequency flow dynamics under coherent gating.

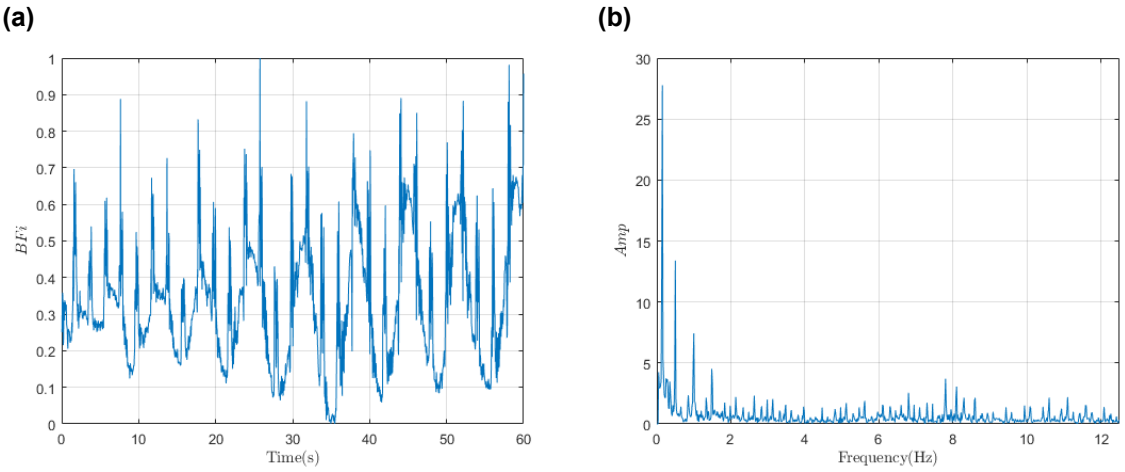

Figure 4.2: LSCI results for $D = 0$ cm with 1 cm phantom (a) Time-domain BFi signal (b) Frequency-domain magnitude spectrum obtained via FFT

Despite subtracting the baseline noise recorded under no-flow conditions, a residual noise component persists—primarily due to the multimode nature of the laser source. This contributes to a constant background in the signal that limits the dynamic range of flow detection.

To further evaluate depth sensitivity, the path length difference D was systematically varied from 0 to 10 cm in 1 mm increments using the same 1 cm thick phantom. At each step, speckle contrast signals

were recorded, and the corresponding SNR was calculated in the frequency domain from the spectral amplitude at the flow modulation frequency.

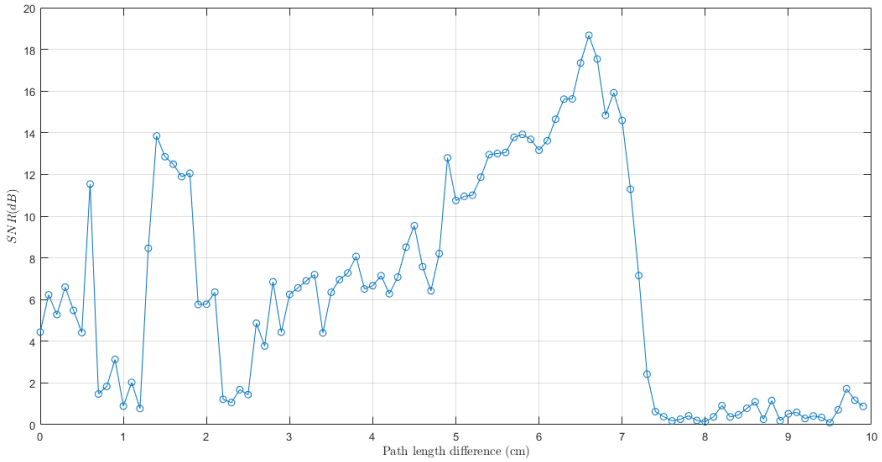

Figure 4.3: SNR as a function of path length difference D for a 1 cm thick phantom

As shown in figure 4.7, a pronounced SNR maximum occurs near $D \approx 6.6\,\mathrm{cm}$, with a peak value of 18.68 dB, indicating the optimal path length difference for coherence-gated flow detection. At this position, the baseline noise is notably suppressed, suggesting that the majority of detected photons originate from deeper tissue layers rather than superficial regions. These deeper layers contribute predominantly dynamic scattering from the flow medium, thereby enhancing signal fidelity while minimizing contamination from static surface scatterers.

The first observable peak in the SNR curve corresponds to the ballistic photons□ those that traverse the medium with minimal scattering. These photons maintain coherence and contribute a sharp interference signal, enabling early detection of superficial flow components. However, beyond this point, the SNR increases as more multiply scattered, dynamically modulated photons from deeper tissue contribute to the detected signal. This optimal gating condition thus reflects the depth at which flow-induced fluctuations are maximally resolved and least affected by stationary interference.

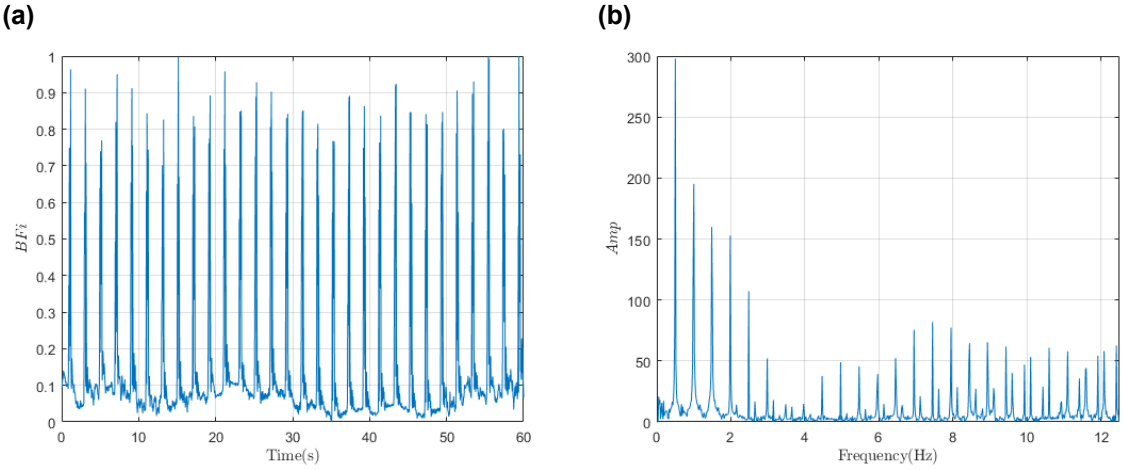

Figure 4.4: LSCI results for $D = 6.6\,\mathrm{cm}$ with 1 cm phantom (a) Time-domain BFi signal (b) Frequency-domain magnitude spectrum obtained via FFT

A minimum SNR threshold of 6 dB is adopted in this study to define the boundary of reliable signal detection, following established benchmarks in speckle-based flow imaging [19, 34, 35]. Measurements

yielding SNR values below this level are considered dominated by noise and thus excluded from further interpretation.

Beyond $D = 7$ cm, the SNR decreases sharply, approaching the detection limit imposed by the coherence properties of the laser source. The furthest detectable coherence gate was observed at $D = 7.2$ cm, where the SNR remained marginally above threshold at 7.12 dB as shown in figure. 4.7. This coherence-limited range sets the upper bound for effective depth-resolved measurements using the current optical setup.

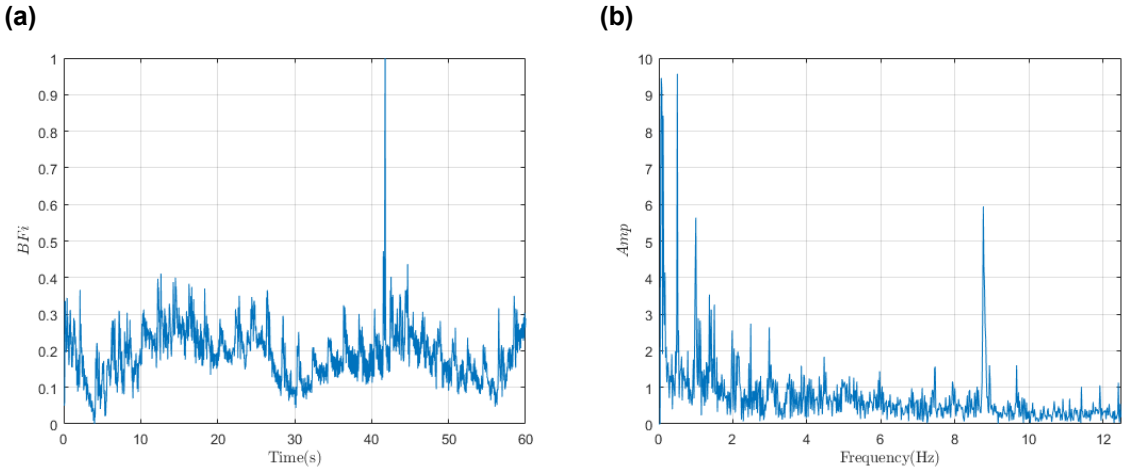

Figure 4.5: LSCI results for $D = 7.2$ cm with 1 cm phantom (a) Time-domain BFi signal (b) Frequency-domain magnitude spectrum obtained via FFT

Increasing the thickness of the phantom to 1.5 cm reveals the depth limitation of the on-axis configuration. As shown in figure 4.6, a measurable signal was observed only at $D = 7$ cm, with a corresponding SNR of 7.83 dB. This value exceeds the 6 dB reliability threshold, but no other depth positions yielded detectable signals above noise level.

The reduction in detectable depth range is attributed to the increased scattering and attenuation experienced by photons as they traverse thicker tissue. With a longer optical path required to reach deeper regions, fewer dynamically scattered photons return within the coherence envelope of the system. This highlights the sensitivity limitation of the on-axis configuration for probing deeper tissue structures. Despite this, the narrow coherence gate at $D = 7$ cm still captures flow-induced speckle fluctuations, as evidenced by the frequency-domain peak in figure 4.6(b).

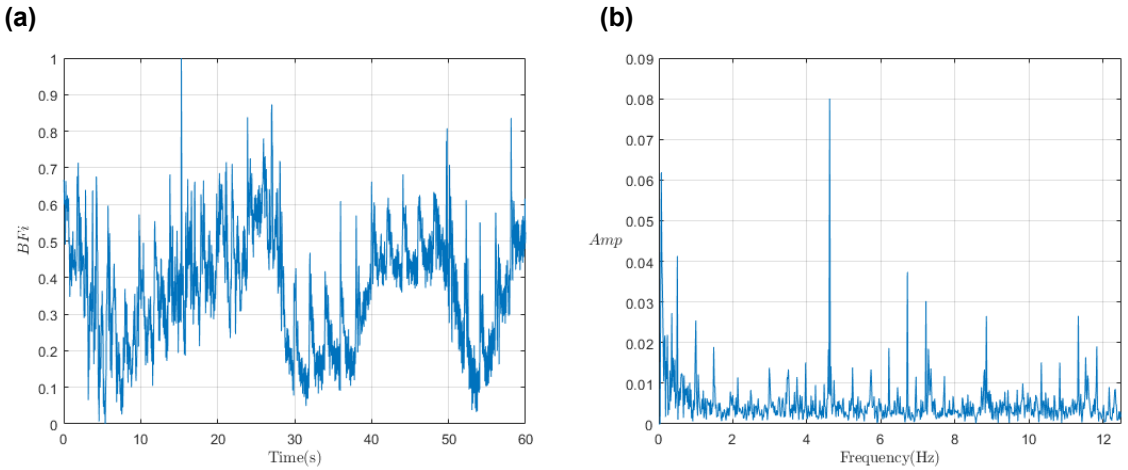

Figure 4.6: LSCI results for $D = 7$ cm with 1.5 cm phantom (a) Time-domain BFi signal (b) Frequency-domain magnitude spectrum obtained via FFT

Another significant limitation observed in the on-axis configuration is the elevated baseline noise, which can be partially attributed to the inherent properties of the multimode laser source. As the optical thickness of the phantom increases, the number of coherently detected photons decreases markedly, resulting in weakened interference fringes and reduced visibility. This attenuation compromises the system's sensitivity to flow-induced speckle fluctuations, which become progressively masked by background noise, thereby diminishing the distinctness of frequency-domain peaks and reducing overall signal fidelity, as demonstrated in figure 4.6(b).

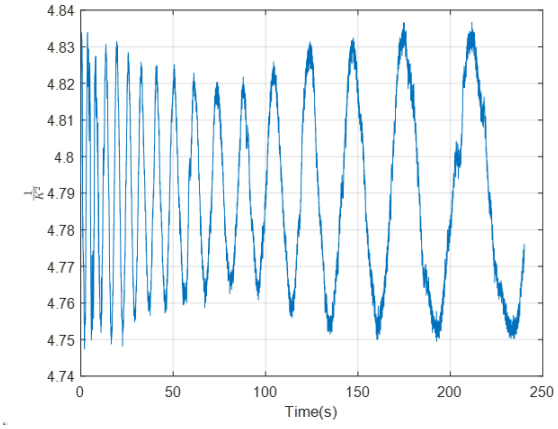

Figure 4.7: Baseline noise in the on-axis configuration

Furthermore, the cumulative effects of multiple scattering events and static backscattering from superficial tissue layers contribute to a persistently elevated noise floor. This complicates the reliable extraction of flow-related spectral components, particularly in deeper or more heterogeneous samples. To mitigate these challenges, one potential approach is the implementation of a dual-camera acquisition system capable of synchronized real-time background subtraction or phase drift compensation. While promising, this solution would entail increased hardware complexity and cost, potentially offsetting the advantages of the current compact and economical design.

4.2. Off-axis Configuration

Relative to the on-axis system—where the camera directly images the sample—the off-axis configuration employs a multimode fiber (FP1000ERT, Thorlabs) placed at a 2 mm source-detector (S–D) separation to collect diffusely scattered light, which is then relayed to the camera. This indirect collection geometry enables more targeted sampling of dynamically scattered photons from deeper tissue layers.

Although the camera remains the final detector in both configurations, the effective numerical aperture (NA) differs due to the fiber's geometry and positioning. The on-axis system, with the camera positioned 7 cm above the sample, captures light through free-space with limited angular acceptance. The effective NA of the camera in the x and y directions is computed as:

$$\mathrm{NA} = n \cdot \sin\theta = \frac{n \cdot (d/2)}{\sqrt{(d/2)^2 + z^2}}, \tag{4.3}$$

where $n = 1.00$ is the refractive index of air, $d = 4.8\,\mathrm{mm}$ or $3.6\,\mathrm{mm}$ is the sensor dimension, and $z = 70\,\mathrm{mm}$ is the distance between the sample and the camera. This yields $\mathrm{NA}_x \approx 0.034$ and $\mathrm{NA}_y \approx 0.026$. In contrast, the fiber offers a much higher numerical aperture of $\mathrm{NA}_{\text{fiber}} = 0.5$, enabling more efficient collection of scattered photons over a wide angular range.

While the camera's large sensor area (27 mm^2) provides high-resolution imaging in the on-axis setup, the angular collection is severely constrained at longer working distances. By comparison, the off-axis fiber, despite its smaller core area (0.25 mm^2), benefits from high NA and proximity to the scattering

site. Taking both area and angular acceptance into account, the theoretical signal gain of the off-axis fiber configuration over the on-axis direct imaging setup is:

$$\text{Gain} \approx \frac{A_{\text{fiber}} \cdot \text{NA}_{\text{fiber}}^2}{A_{\text{CMOS}} \cdot \text{NA}_x \cdot \text{NA}_y} = \frac{0.25 \cdot 0.5^2}{27 \cdot 0.034 \cdot 0.026} \approx 2.61. \tag{4.4}$$

This suggests that, under the current setup, routing collection through a high-NA fiber enhances photon throughput and improves sensitivity to deep flow signals. To experimentally validate this theoretical gain, we compared the photon throughput of the on-axis and off-axis configurations under identical illumination and acquisition conditions. A 100 mW laser diode was used to illuminate a 1 cm thick tissue-mimicking phantom, with both configurations operating at an exposure time of 1/106 s. The optical path length difference was fixed at $D = 0\,\text{cm}$. Each system collected continuous image data over a 60-second interval.

For each acquired frame, we computed the average pixel intensity across the sensor to quantify the total detected signal. The off-axis configuration—utilizing a 1000 μm core fiber at a 2 mm source-detector (S–D) separation—delivered a higher and more stable photon count per frame, confirming the enhanced collection efficiency afforded by the high-NA fiber as figure below shown.

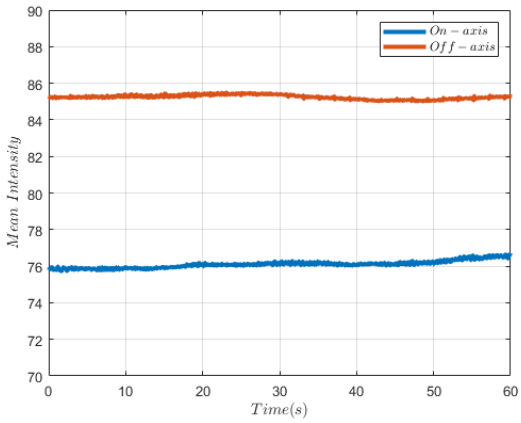

Figure 4.8: Average intensity of camera for on-axis and off-axis configuration

This enhanced photon throughput was further evidenced using a 2 cm thick phantom, where the off-axis configuration continued to yield robust flow signals, while the on-axis system exhibited a marked reduction in signal fidelity. The sustained performance in highly scattering media highlights the off-axis system's superior depth sensitivity and resilience to attenuation, aligning with the theoretical predictions based on geometric and angular collection advantages.

Next, we characterized the performance advantage of the off-axis system relative to the on-axis configuration. Under identical illumination and acquisition parameters—including a matched-arm condition ($D = 0\,\text{cm}$), a 1 cm-thick phantom, and a pump modulation period of 2 s—time-resolved speckle signals were recorded over a 60-second interval. LSCI was applied to compute contrast-based blood flow index (BFi), and ISVS was subsequently used to extract dynamic visibility modulations.

Figure 4.2 shows the result of applying LSCI to the on-axis system. Although a periodic component is present in the time domain (a), the frequency-domain FFT spectrum (b) reveals a lower peak amplitude and elevated noise floor, indicating reduced signal fidelity and weaker flow modulation contrast. The calculated signal-to-noise ratio (SNR) was below 6 dB for most frequency components, suggesting suboptimal sensitivity.

In contrast, the off-axis configuration demonstrated improved robustness and enhanced SNR. As shown in figure 4.9, the LSCI signal reveals a strong pattern aligned with the 2 s modulation cycle, and the FFT exhibits a prominent peak near 0.5 Hz with low background noise. The measured SNR reached 14.48 dB, exceeding the 6 dB threshold for reliable flow detection.

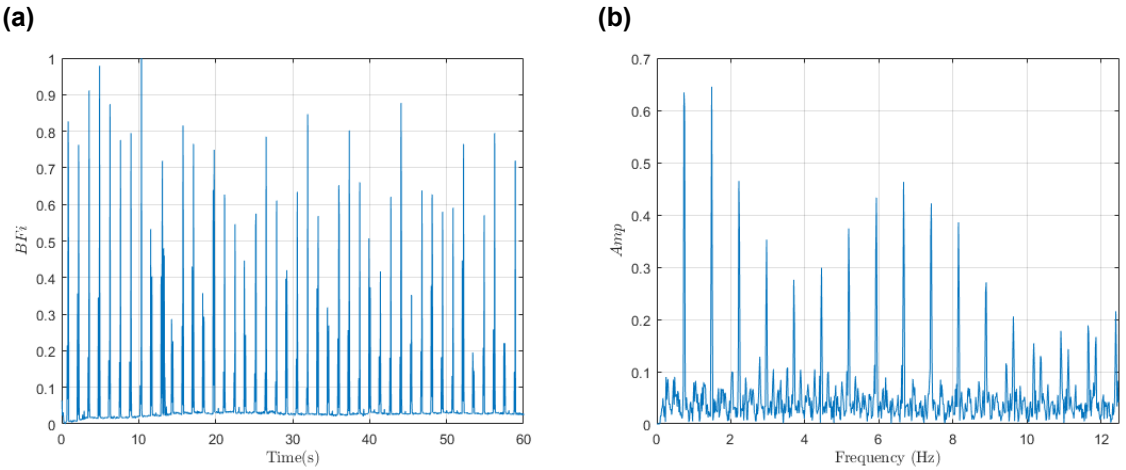

Figure 4.9: LSCI results for $D = 0$ cm with 1 cm phantom: (a) Time-domain BFi signal; (b) Frequency-domain magnitude spectrum obtained via FFT.

ISVS analysis was also applied to the off-axis configuration. figure 4.10(a) shows a stable time-domain BFi waveform with clear periodicity, while figure 4.10(b) demonstrates sharp spectral content centered at the 0.5 Hz modulation frequency, indicating strong signal reproducibility and low noise contamination. The measured SNR reached 15.97 dB, exceeding the 6 dB threshold for reliable flow detection.

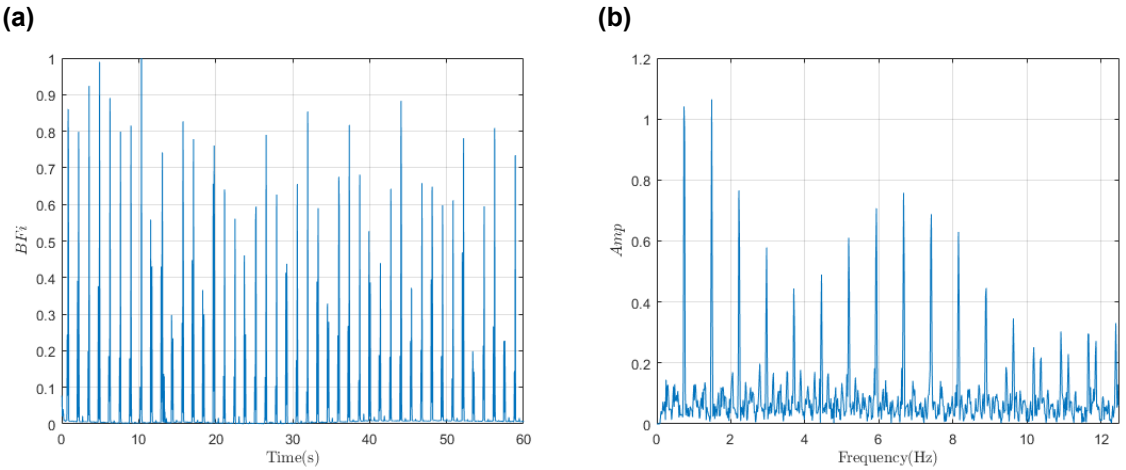

Figure 4.10: ISVS results for $D = 0$ cm with 1 cm phantom: (a) Time-domain BFi signal; (b) Frequency-domain magnitude spectrum obtained via FFT.

Together, these results highlight the performance benefits of the off-axis scheme. Although the camera-based on-axis system is simpler in geometry, it suffers from reduced depth sensitivity and temporal SNR under equivalent conditions. By leveraging the larger angular acceptance and direct photon collection of the fiber, the off-axis configuration achieves higher signal fidelity and robust flow detection—even within short integration windows—demonstrating its utility for dynamic speckle-based flow imaging.

To further evaluate the depth sensitivity of the off-axis system, we systematically varied the optical path length difference D from 0 to 30 cm in 1 cm increments while maintaining a fixed phantom thickness of 1 cm. At each depth setting, speckle contrast signals were acquired under consistent illumination and modulation conditions. Both LSCI and ISVS were employed to extract dynamic flow fluctuations, and the corresponding signal-to-noise ratio (SNR) was calculated based on the amplitude of the Fourier component at the flow modulation frequency. The pump was operated at a cycle period of approximately 1.5 s, corresponding to a modulation frequency of 0.67 Hz.

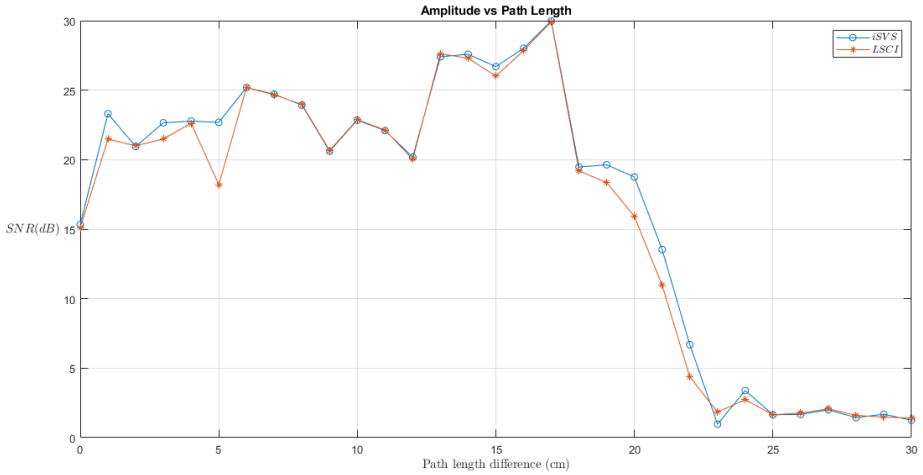

Figure 4.11: SNR as a function of path length difference D for a 2 cm-thick phantom, comparing ISVS and LSCI methods.

As shown in figure 4.11, both methods provided reliable signals with SNR exceeding 20 dB up to a moderate depth. Notably, both LSCI and ISVS achieved their maximum SNR values near 17 cm, with LSCI slightly outperforming ISVS—29.93 dB vs. 29.17 dB. The BFi traces from both techniques at this depth appear nearly identical, demonstrating excellent temporal coherence and flow signal clarity.

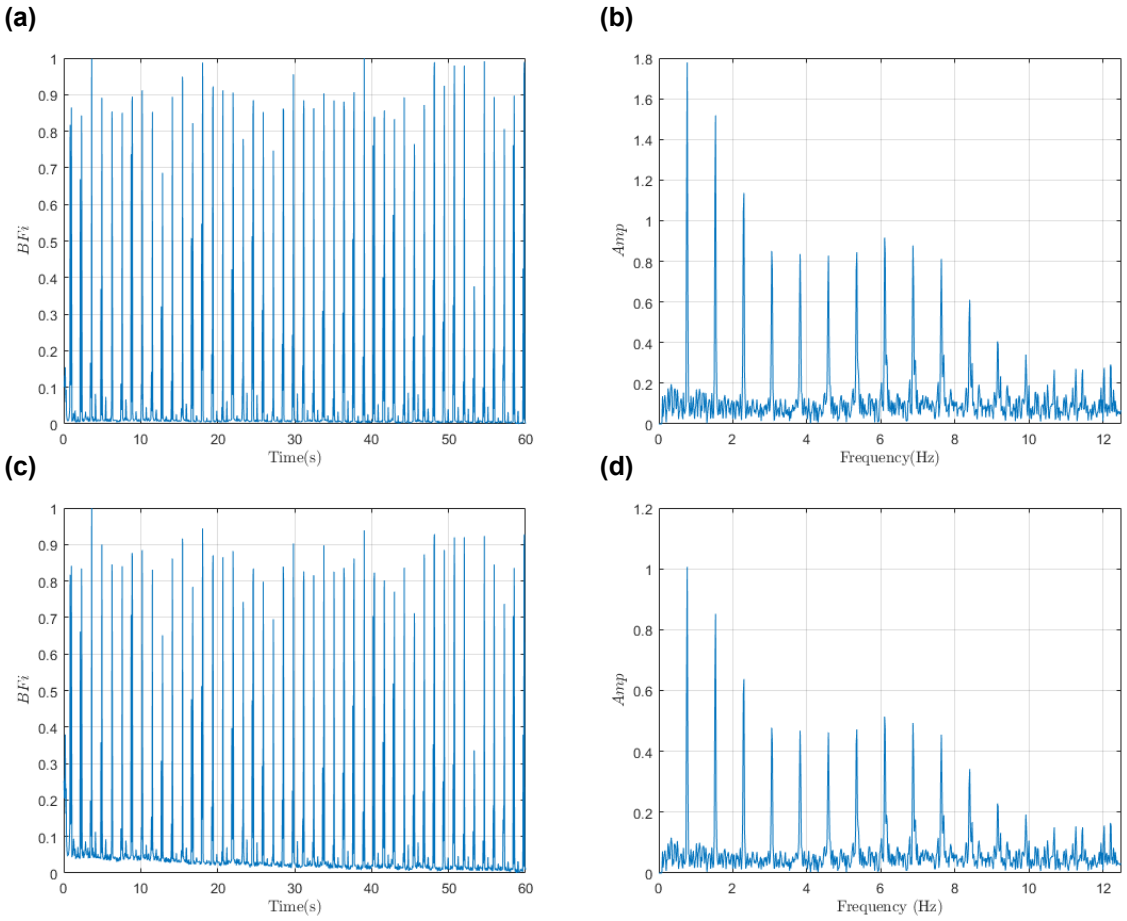

Figure 4.12: Comparison of ISVS and LSCI performance at maximum SNR (D = 17 cm) for 1 cm phantom: (a,b) ISVS time and frequency domain; (c,d) LSCI time and frequency domain.

At extended path length differences, ISVS retained detectable signals with higher fidelity. At $D = 21\,\mathrm{cm}$, ISVS maintained an SNR of 13.53 dB, clearly above the 6 dB threshold for reliable detection. In contrast, LSCI at the same depth dropped to 10.96 dB, approaching the noise floor and exhibiting reduced modulation visibility.

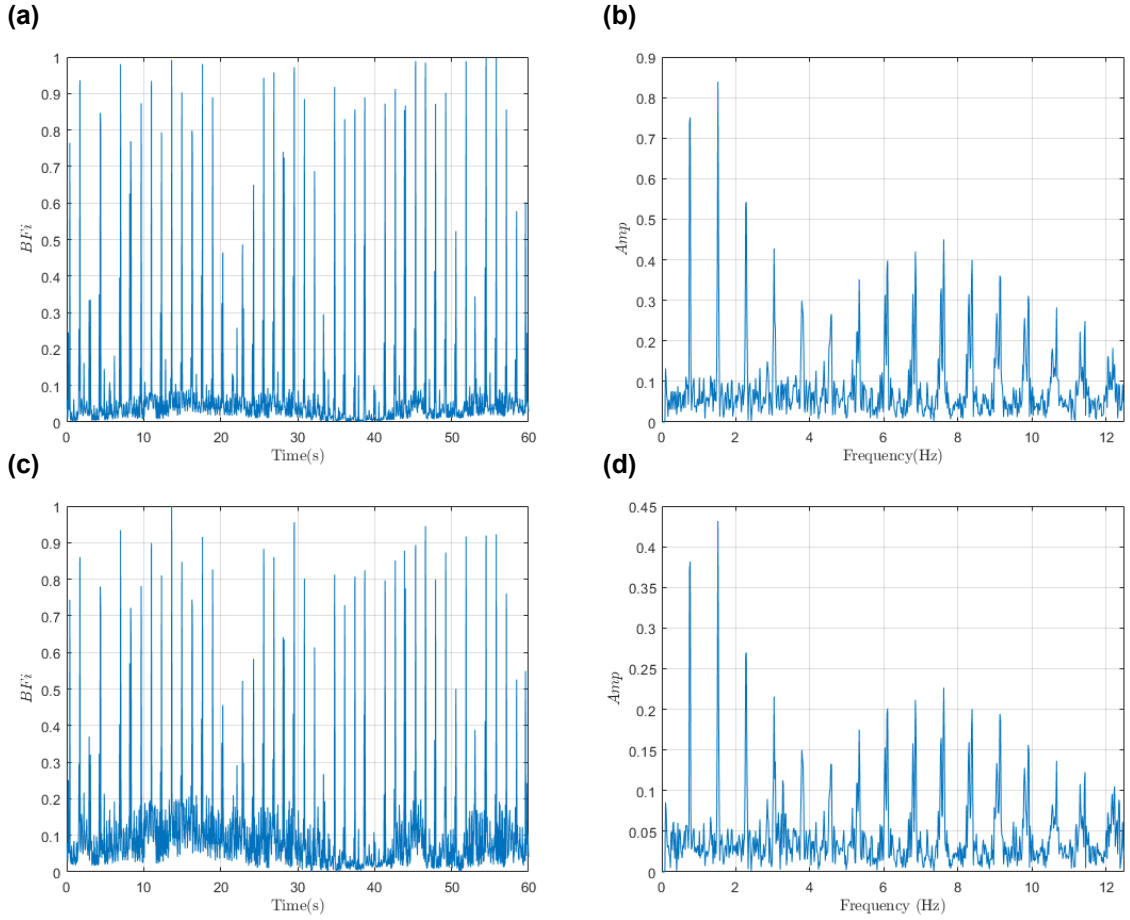

Figure 4.13: Comparison of ISVS and LSCI performance at the furthest measurable depth (D = 21 cm) for 1 cm phantom: (a,b) ISVS time and frequency domain; (c,d) LSCI time and frequency domain.

To further evaluate the depth sensitivity of the off-axis system, we systematically varied the optical path length difference D from 0 to 30 cm in 1 cm increments while testing two phantom thicknesses: 1.5 cm and 2 cm. At each depth, speckle contrast signals were recorded under identical illumination and modulation conditions. Both LSCI and ISVS methods were applied to extract flow dynamics, with signal-to-noise ratio (SNR) quantified from the Fourier amplitude at the modulation frequency.

As shown in Figure 4.14, for the 1.5 cm-thick phantom, both LSCI and ISVS achieved high SNR ($> 20\,\mathrm{dB}$) for path length differences up to approximately 9 cm. The maximum SNR occurred at $D = 10\,\mathrm{cm}$, where ISVS marginally outperformed LSCI (25.29 dB vs. 24.17 dB). Beyond this point, however, ISVS maintained significantly higher SNR at extended depths. While both techniques detected signal up to $D = 18\,\mathrm{cm}$, ISVS sustained an SNR of 13.14 dB compared to 7.78 dB for LSCI. This demonstrates ISVS's superior resilience in deeper, turbid regimes, which can be attributed to its unnormalized signal extraction strategy—preserving the full magnitude of flow-related fluctuations while minimizing stationary and coherence-induced noise.

With a 2 cm-thick phantom (Figure 4.15), both methods experienced an overall SNR reduction due to increased scattering and attenuation. Peak values were again observed at $D = 10\,\mathrm{cm}$, with ISVS yielding 20.83 dB and LSCI 19.73 dB. As depth increased, the SNR for both methods declined, but ISVS maintained a stronger signal across all deeper path lengths. At $D = 17\,\mathrm{cm}$, ISVS and LSCI measured 11.12 dB and 7.72 dB respectively—further highlighting ISVS's improved depth performance. These

results confirm that ISVS offers greater sensitivity and robustness under highly scattering conditions, making it a preferred approach for deep-tissue hemodynamic imaging.

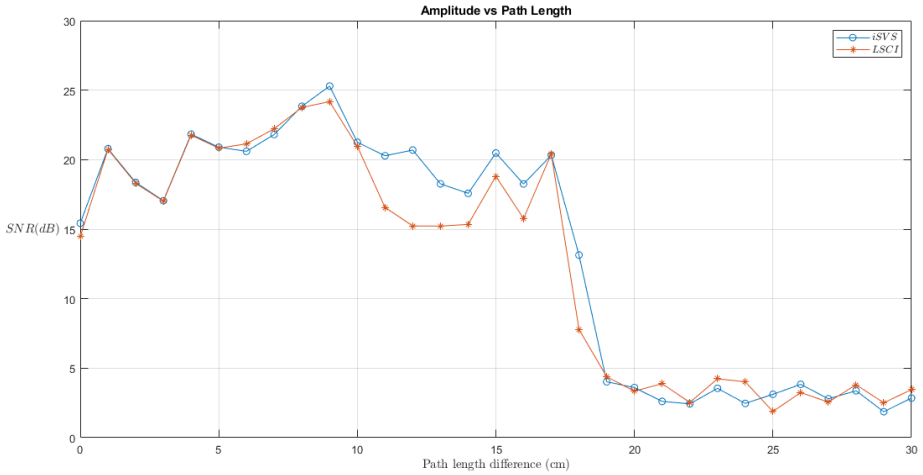

Figure 4.14: SNR as a function of path length difference D for a 1.5 cm-thick phantom, comparing ISVS and LSCI methods.

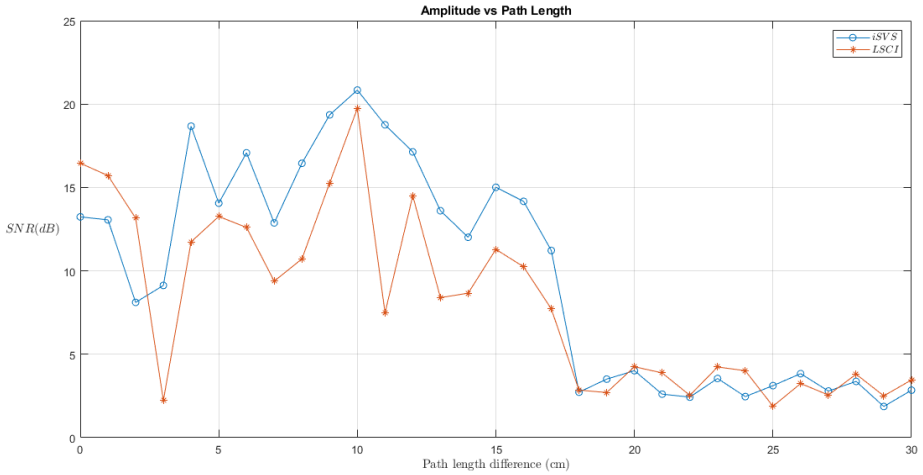

Figure 4.15: SNR as a function of path length difference D for a 2 cm-thick phantom, comparing ISVS and LSCI methods.

The detailed figures for peak SNR and longest detectable D are provided in Appendix B.

4.2.1. Discussion

The off-axis configuration demonstrates a substantial enhancement in photon collection efficiency, offering a 2.6-fold increase compared to the conventional on-axis geometry. This theoretical expectation was empirically validated using a 1 cm-thick tissue-mimicking phantom under matched illumination and acquisition conditions. The off-axis system consistently yielded signals of higher intensity and improved temporal stability, thereby confirming its enhanced photon throughput and superior sensitivity to deeper scattering layers.

As illustrated in figures 4.14–4.15, both Laser Speckle Contrast Imaging (LSCI) and interferometric Spatial Variance Sensing (iSVS) exhibit comparable signal-to-noise ratio (SNR) characteristics in regimes involving short optical path length differences ($D < 10\,\mathrm{cm}$), where ballistic and quasi-ballistic photons dominate the detected signal. Within this range, LSCI occasionally demonstrates marginally superior

peak SNR values, which can be attributed to its utilization of full-frame spatial averaging that effectively mitigates stochastic noise components.

With increasing phantom thickness, a systematic forward shift in the location of maximum SNR is observed—from approximately 17 cm for 1 cm-thick phantoms to near 10 cm for 2 cm-thick samples. This shift is indicative of a reduced effective coherence gating depth, arising from increased scattering and attenuation. Concurrently, both the peak SNR and the maximum depth at which reliable signal retrieval is feasible decline, aligning with theoretical expectations regarding photon diffusion and signal degradation in turbid media.

These findings further reinforce the robustness of iSVS in optically dense environments. The method's resilience is principally attributed to its capacity to suppress DC and static components, thereby attenuating noise arising from coherence fluctuations in multimode laser illumination. This selective sensitivity to dynamic scattering enhances the detectability of flow-induced modulations under highly scattering conditions.

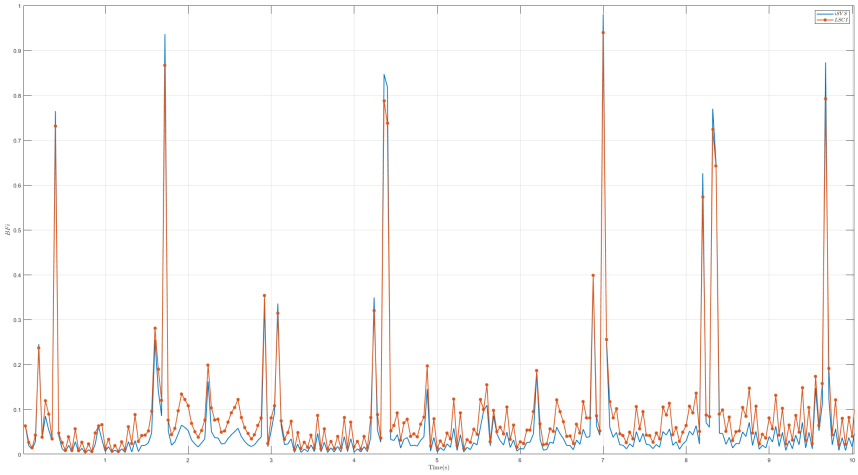

Figure 4.16: Comparison of iSVS and LSCI methods for BFi estimation.

Furthermore, LSCI also shows poor robustness to mechanical disturbances. Vibration, which may be caused by the optical platform, can impose spurious fluctuations on speckle intensity that can be mistaken for true hemodynamic signals. Even though temporal filtering can help suppress much of this background, baseline instability usually persists, as seen in Figure 4.16, in which the LSCI signal shows an unstable and variable baseline with superimposed high-amplitude spiking.

Conversely, iSVS exhibits enhanced resistance to such disturbances, due to its intrinsic capability to attenuate low-frequency content commonly related to mechanical movement. Even without filtering, the signal from iSVS is comparatively stable, and subsequent processing increases temporal smoothness without altering physiological trends. This stability emphasizes the enhanced artifact rejection capability of iSVS, particularly in mechanically noisy environments.

Even though minute variations in either of both modalities are possible owing to intrinsic instabilities of the light source, iSVS always delivers extremely reproducible results across several measurements, further confirming its robustness and physiological reliability.

In summary, iSVS provides several advantages in mechanical stability, depth range, and depth sensitivity, which suit it especially well for deep-tissue imaging in hostile environments. While LSCI continues to be desirable for its simplicity and ease of use, iSVS, provides a more optimal platform for high-fidelity hemodynamic imaging in settings where mechanical isolation is not easily achieved.

5

Conclusion

This study has presented a comprehensive evaluation of a cerebral blood flow (CBF) measurement system incorporating both on-axis and off-axis detection geometries, augmented by a coherence-based time-of-flight (ToF) gating mechanism. By precisely tuning the optical path length difference (OPD) between the sample and reference arms, the system enables selective interference of photons with specific time-of-flight characteristics. This approach facilitates operation at short source–detector (S–D) separations, thereby enhancing spatial resolution and photon throughput without compromising sensitivity to deeper tissue layers. The resulting platform constitutes a scalable, cost-effective solution for high-resolution, depth-resolved CBF imaging in scattering biological media.

In particular, the integration of a high-numerical-aperture (NA) fiber optic collection system within the off-axis configuration markedly improves photon harvesting efficiency, yielding a theoretical 2.6-fold enhancement in throughput compared to the on-axis architecture. This theoretical advantage was experimentally validated across tissue-mimicking phantoms, where the off-axis geometry consistently produced higher-intensity signals with improved temporal stability, confirming its superior photon collection capability and enhanced sensitivity to deeper scattering layers.

Across a range of phantom thicknesses, both Laser Speckle Contrast Imaging (LSCI) and interferometric Spatial Variance Sensing (iSVS) exhibited the expected decline in signal-to-noise ratio (SNR) with increasing depth. At short OPDs, where ballistic and quasi-ballistic photons dominate, LSCI occasionally achieved slightly higher peak SNR due to full-frame spatial averaging. However, as scattering and attenuation increased, iSVS maintained measurable signal content at greater OPDs, reflecting its resilience in highly scattering environments and its ability to suppress static background contributions and coherence-related noise from multimode illumination.

Mechanical stability revealed a clear distinction between the modalities: iSVS demonstrated superior robustness to mechanical perturbations, with signals remaining stable even in the presence of structural vibrations, whereas LSCI exhibited baseline drift under same conditions. These findings highlight iSVS's enhanced artifact rejection in mechanically unstable environments, further reinforcing its suitability for challenging experimental settings.

Overall, the comparative results underscore the complementary strengths of the two methods. LSCI offers simplicity, ease of implementation, and strong performance at superficial depths, while iSVS integrated with coherence gating—provides greater depth sensitivity, improved robustness in scattering and mechanically noisy conditions, and more reliable hemodynamic measurements in complex imaging environments.

The transition to *in vivo* application represents the next critical stage in system development. A redesigned sample arm will be introduced to enhance mechanical robustness and ensure user safety within dynamic clinical environments. Laser illumination will be delivered through a multimode optical fiber, with the distal tip positioned a few millimeters above the scalp or skin surface. This configuration maintains a fixed source–detector separation and ensures irradiance levels remain compliant with

ANSI safety standards, even under conditions of subject motion.

Together, these planned enhancements are intended to support the translation of the platform into a practical, non-invasive, motion-resilient, and depth-resolved neurovascular monitoring tool suitable for both clinical and preclinical applications.

References

[1] H Girouard and C Iadecola. “Neurovascular coupling in the normal brain and in hypertension, stroke, and Alzheimer disease”. In: *Journal of Applied Physiology (1985)* 100.1 (2006), pp. 328–335. DOI: 10.1152/japplphysiol.00966.2005.

[2] Wenjun Zhou et al. “Highly parallel, interferometric diffusing wave spectroscopy for monitoring cerebral blood flow dynamics”. In: *Optica* 5 (2018), pp. 518–527. DOI: 10.1364/OPTICA.5.000518.

[3] G. E. Strangman, Z. Li, and Q. Zhang. “Depth sensitivity and source-detector separations for near infrared spectroscopy based on the Colin27 brain template”. In: *PLoS One* 8.8 (2013), e66319. DOI: 10.1371/journal.pone.0066319.

[4] S. A. Carp, M. B. Robinson, and M. A. Franceschini. “Diffuse correlation spectroscopy: current status and future outlook”. In: *Neurophotonics* 10.1 (2023), p. 013509. DOI: 10.1117/1.NPh.10.1.013509.

[5] David A Boas and Andrew K Dunn. “Laser speckle contrast imaging in biomedical optics”. In: *Journal of Biomedical Optics* 15.1 (2010), p. 011109. DOI: 10.1117/1.3285504.

[6] Janaka Senarathna, A Rege, Nan Li, et al. “Laser speckle contrast imaging: Theory, instrumentation and applications”. In: *IEEE Reviews in Biomedical Engineering* (2013). DOI: 10.1109/RBME.2012.2235496.

[7] MM Qureshi et al. “Advances in laser speckle imaging: From qualitative to quantitative hemodynamic assessment”. In: *Journal of Biophotonics* (2024). DOI: 10.1002/jbio.202300126.

[8] F Fathi, S Mazdeyasna, D Singh, et al. “Time-resolved Laser Speckle Contrast Imaging (TR-LSCI) of Cerebral Blood Flow”. In: *IEEE Transactions on Medical Imaging* (2024). DOI: 10.1109/TMI.2024.10734408.

[9] C. Huang et al. “Low-cost compact diffuse speckle contrast flowmeter using small laser diode and bare charge-coupled-device”. In: *Journal of Biomedical Optics* 21.8 (2016), p. 080501. DOI: 10.1117/1.JBO.21.8.080501.

[10] X. Liu et al. “Simultaneous measurements of tissue blood flow and oxygenation using a wearable fiber-free optical sensor”. In: *Journal of Biomedical Optics* 26.1 (2021), p. 012705. DOI: 10.1117/1.JBO.26.1.012705.

[11] M. Ghijsen et al. “Wearable speckle plethysmography (SPG) for characterizing microvascular flow and resistance”. In: *Biomedical Optics Express* 9.8 (2018), p. 3937. DOI: 10.1364/BOE.9.003937.

[12] F. Bonetta-Misteli et al. “Development and evaluation of a wearable peripheral vascular compensation sensor in a swine model of hemorrhage”. In: *Biomedical Optics Express* 14.10 (2023), p. 5338. DOI: 10.1364/BOE.493675.

[13] J. Herranz Olazabal et al. “Comparison between speckle plethysmography and photoplethysmography during cold pressor test referenced to finger arterial pressure”. In: *Sensors* 23.11 (2023), p. 5016. DOI: 10.3390/s23115016.

[14] C Huang et al. “Noninvasive noncontact speckle contrast diffuse correlation tomography of cerebral blood flow in rats”. In: *NeuroImage* (2019). DOI: 10.1016/j.neuroimage.2019.06.020.

[15] T Dragojević, JL Hollmann, and D Tamborini. “Compact, multi-exposure speckle contrast optical spectroscopy (SCOS) device for measuring deep tissue blood flow”. In: *Biomedical Optics Express* 9.1 (2017), pp. 322–336. DOI: 10.1364/BOE.9.000322.

[16] J Xu et al. “Interferometric speckle visibility spectroscopy (ISVS) for human cerebral blood flow monitoring”. In: *APL Photonics* 5.12 (2020), p. 126102. DOI: 10.1063/5.0028093.

[17] S Mahler et al. “Assessing depth sensitivity in laser interferometry speckle visibility spectroscopy (iSVS) through source-to-detector distance variation and cerebral blood flow monitoring in humans and rabbits”. In: *Biomedical Optics Express* 14.9 (2023), pp. 4964–4978. DOI: 10.1364/BOE.14.004964.

[18] YX Huang, S Mahler, and M Dickson. “Compact and cost-effective laser-powered speckle contrast optical spectroscopy fiber-free device for measuring cerebral blood flow”. In: *Journal of Biomedical Optics* 29.6 (2024), p. 067001. DOI: 10.1117/1.JBO.29.6.067001.

[19] David A Boas et al. “Establishing the diffuse correlation spectroscopy signal relationship with blood flow”. In: *Neurophotonics* 3.3 (2016), pp. 031412–031412. DOI: 10.1117/1.NPh.3.3.031412.

[20] K Jeong, JJ Turek, and DD Nolte. “Fourier-domain digital holographic optical coherence imaging of living tissue”. In: *Applied Optics* 46.22 (2007), pp. 4999–5005. DOI: 10.1364/AO.46.004999.

[21] L Colombo, M Pagliazzi, and S Konugolu Venkata Sekar. “In vivo time-domain diffuse correlation spectroscopy above the water absorption peak”. In: *Optics Letters* (2020). DOI: 10.1364/OL.45.003377.

[22] V Parfentyeva et al. “Fast time-domain diffuse correlation spectroscopy with superconducting nanowire single-photon detector: system validation and in vivo results”. In: *Scientific Reports* (2023). DOI: 10.1038/s41598-023-39281-5.

[23] S Samaei et al. “Time-domain diffuse correlation spectroscopy (TD-DCS) for noninvasive, depth-dependent blood flow quantification in human tissue in vivo”. In: *Scientific Reports* (2021). DOI: 10.1038/s41598-021-81448-5.

[24] Quan Wang et al. “A comprehensive overview of diffuse correlation spectroscopy: Theoretical framework, recent advances in hardware, analysis, and applications”. In: *NeuroImage* 298 (2024), p. 120793. ISSN: 1053-8119. DOI: 10.1016/j.neuroimage.2024.120793.

[25] M Mohtasebi et al. “Depth-sensitive diffuse speckle contrast topography for high-density mapping of cerebral blood flow in rodents”. In: *Neurophotonics* 10.4 (2023), p. 045007. DOI: 10.1117/1.NPh.10.4.045007.

[26] D. Botez, D. Z. Garbuzov, and G. J. Davies. “High-power broad-area diode lasers”. In: *IEEE Journal of Selected Topics in Quantum Electronics* 11.3 (2005), pp. 659–676. DOI: 10.1109/JSTQE.2005.850600.

[27] C. Pflügl et al. “Low-coherence, high-brightness quantum cascade lasers”. In: *Optics Letters* 34.3 (2009), pp. 287–289. DOI: 10.1364/OL.34.000287.

[28] T. Numai. *Fundamentals of Semiconductor Lasers*. Springer, 2004. ISBN: 9780387400765. DOI: 10.1007/978-0-387-40077-2.

[29] Aaron M. Goldfain et al. “Polydimethylsiloxane tissue□mimicking phantoms with tunable optical properties”. In: *Journal of Biomedical Optics* 27.7 (2022), p. 074706. DOI: 10.1117/1.JBO.27.7.074706.

[30] L. Xu, A. K. Jahromi, and C. Yang. “Diffusing wave spectroscopy: A unified treatment on temporal sampling and speckle ensemble methods”. In: *APL Photonics* 6.1 (2021), p. 016105. DOI: 10.1063/5.0034576.

[31] A. Goldfain et al. “Polydimethylsiloxane tissue-mimicking phantoms with tunable optical properties”. In: *Biomedical Optics Express* 11.3 (2020), pp. 1644–1656. DOI: 10.1364/BOE.382747.

[32] James R Janesick et al. “Scientific charge-coupled devices”. In: *Optical Engineering* 26.8 (1987), pp. 692–714.

[33] William Fleetwood Sheppard. “On the calculation of the most probable values of frequency-constants, for data arranged according to equidistant division of a scale”. In: *Proceedings of the London Mathematical Society* 1.1 (1897), pp. 353–380.

[34] Hao Cheng, Yu Yan, and Timothy Q Duong. “Temporal statistical analysis of laser speckle images and its application to retinal blood-flow imaging”. In: *Optics Express* 16.14 (2008), pp. 10214–10219. DOI: 10.1364/OE.16.010214.

[35] Pavel Zakharov et al. “Interferometric optical signal detection in the presence of speckle noise”. In: *Optics Letters* 35.20 (2010), pp. 3412–3414. DOI: 10.1364/OL.35.003412.

A

Source Code

```
%% LSCI
clc;
close all;
clear;

%% Parameters
gain = 34;                    % Camera gain
CF = 5.13;                    % Conversion Factor
gamma = gain / CF;
sigma_cam_sq = 15.2;          % Camera noise

%% Read image sequence
image_folder = './R/';
image_files = dir(fullfile(image_folder, '*.jpg'));
num_frames = length(image_files);
K_s_adjusted = zeros(num_frames, 1);
t = 1:num_frames;

%% Load and prepare background
background_img = imread("2-13\L808P200\3\12\Background.bmp");
background_img = gpuArray(double(background_img));

%% Process each image
for i = 1:num_frames
    image_path = fullfile(image_folder, image_files(i).name);
    img = imread(image_path);

    img = gpuArray(double(img));
    img = img - background_img;
    img = max(img, 0);  % Avoid negative values

    %% Global mean and variance
    mu_I = mean(img(:));
    var_I = var(img(:));

    %% Raw K^2
    K2_raw = var_I / (mu_I^2 + eps);

    %% Noise correction
    K2_shot  = gamma / (mu_I + eps);
    K2_quant = 1 / (12 * (mu_I^2 + eps));
    K2_cam   = sigma_cam_sq / (mu_I^2 + eps);

    %% Adjusted K^2
    K2_adjusted = K2_raw - K2_shot - K2_quant - K2_cam;

    %% Store result
    K_s_adjusted(i) = gather(K2_adjusted);
end
```

```

%% Plot result
figure
plot(t/25, K_s_adjusted, 'k-', 'LineWidth', 1.5);
xlabel('Time␣(s)');
ylabel('$K^2_{\rm␣adjusted}$', 'Interpreter', 'latex');
title('Noise-Corrected␣Speckle␣Contrast␣(Global)');
grid on;
```

```
%% ISVS
clc;
close all;
clear;
%% Read
image_folder = './2/';
image_files = dir(fullfile(image_folder, '*.jpg'));

fft_folder = './0/FFT/';
num_frames = length(image_files);

K = zeros(num_frames, 1);
F = zeros(num_frames, 1);
t = 1:num_frames;

background_img = imread("REF.jpg");
background_img = gpuArray(double(background_img));
Ir = mean(background_img(:));
%% Fliter
mask1 = zeros(960, 1280);
mask2 = zeros(960, 1280);

center_x = 146;
center_y = 501;
a = 146;
b = 125;
[x, y] = meshgrid(1:1280, 1:960);
mask1(((x - center_x).^2) / a^2 + ((y - center_y).^2) / b^2 <= 1) = 1;
offset = [481-center_y, 641-center_x];

center_x = 641;
center_y = 481;
a2 = 300;
b2 = 250;
mask2(((x - center_x).^2) / a2^2 + ((y - center_y).^2) / b2^2 <= 1) = 1;
%% Process
for i = 1:num_frames
    img = imread(fullfile(image_folder, image_files(i).name));
    img = gpuArray(double(img));
    K(i) = gather(std(img(:)) / mean(img(:)));

    % img = img - background_img;
    % img = max(img, 0);

    img_fft = fftshift(fft2(img));

    % fft_image_filename = fullfile(fft_folder, ['fft_', num2str(i), '.png']);
    % fft_log = log(1 + abs(img_fft));
    % fft_norm = mat2gray(gather(abs(fft_log)));
    % imwrite(fft_norm, fft_image_filename);

    lobe = img_fft .* mask1;
    lobe = circshift(lobe, offset);
    energy_S = sum(abs(lobe(:)).^2);

    % img_ifft = ifftshift(lobe);
    % img_ifft = ifft2(img_ifft);
    % img_ifft = abs(img_ifft);
    % energy_S = mean(img_ifft(:));

    % img_DC = img_fft .* mask2;
    % img_DC = ifftshift(img_DC);
```

```
    % img_DC = ifft2(img_DC);
    % Is = mean(abs(img_DC(:)));
    % Is = mean(abs(img_DC(:)).^2);
    % Is = sum(abs(img_DC(:)).^2);

    F(i) = gather(energy_S);
    % K(i) = gather(std(img_ifft(:))/mean(img_ifft(:)));
end
%% Plot
exposure_time = 1/106;
beta = 0.75;

windowSize = 10;
F_f = movmean(F, windowSize);
K_f = movmean(K, windowSize);

F_min = min(F);
F_max = max(F);
B =  (F_max - F_min) / (F - F_min);
% F_scaled = F_norm * (0.95 - 0.3) + 0.3;
%
% tau_grid = logspace(-6, 0.5, 5000);
% T = exposure_time;
% F_model = (1 - beta) + beta * (2 * tau_grid / T) .* (1 + (tau_grid / T) .* (exp(-T ./
    tau_grid) - 1));
% tau_interp = interp1(F_model, tau_grid, F_scaled, 'linear', 'extrap');
% BFI = 1 ./ tau_interp;

figure;
semilogy(t/25, 1./F);
hold on
semilogy(t/25, 1./F_f);
legend('$Raw$','$Fit$','Interpreter', 'latex')
xlabel('$Time␣(s)$', 'Interpreter', 'latex');
ylabel('$Amplitude$', 'Interpreter', 'latex');
title('Blood␣Flow␣Index␣via␣iSVS');
grid on;

figure;
plot(t/25, 1./K.^2);
hold on
plot(t/25, 1./K_f.^2);
legend('$Raw$','$Fit$','Interpreter', 'latex')
xlabel('$Time␣(s)$', 'Interpreter', 'latex');
ylabel('$Amplitude$', 'Interpreter', 'latex');
title('Blood␣Flow␣Index␣via␣LSCI');
grid on;

N = length(t);
f = (-N/2:N/2-1) * (25 / N);
% F_detrended = detrend(F);
I = fftshift(fft(F));
I = abs(I);
I(f < 0.05) = 0;

I_K = fftshift(fft(K));
I_K = abs(I_K);
I_K(f < 0.05) = 0;

figure;
plot(f, I, 'LineWidth', 1);
xlim([0 12.5]);
xlabel('$Frequency␣(Hz)$', 'Interpreter', 'latex');
ylabel('$Amplitude$', 'Interpreter', 'latex');
title('Frequency␣Spectrum␣of␣Visibility␣Signal');
grid on;

figure;
plot(f, I_K, 'LineWidth', 1);
xlim([0 12.5]);
xlabel('$Frequency␣(Hz)$', 'Interpreter', 'latex');
```

```
133 ylabel('$Amplitude$', 'Interpreter', 'latex');
134 title('Frequency␣Spectrum␣of␣Contrast');
135 grid on;
```

B

Figures

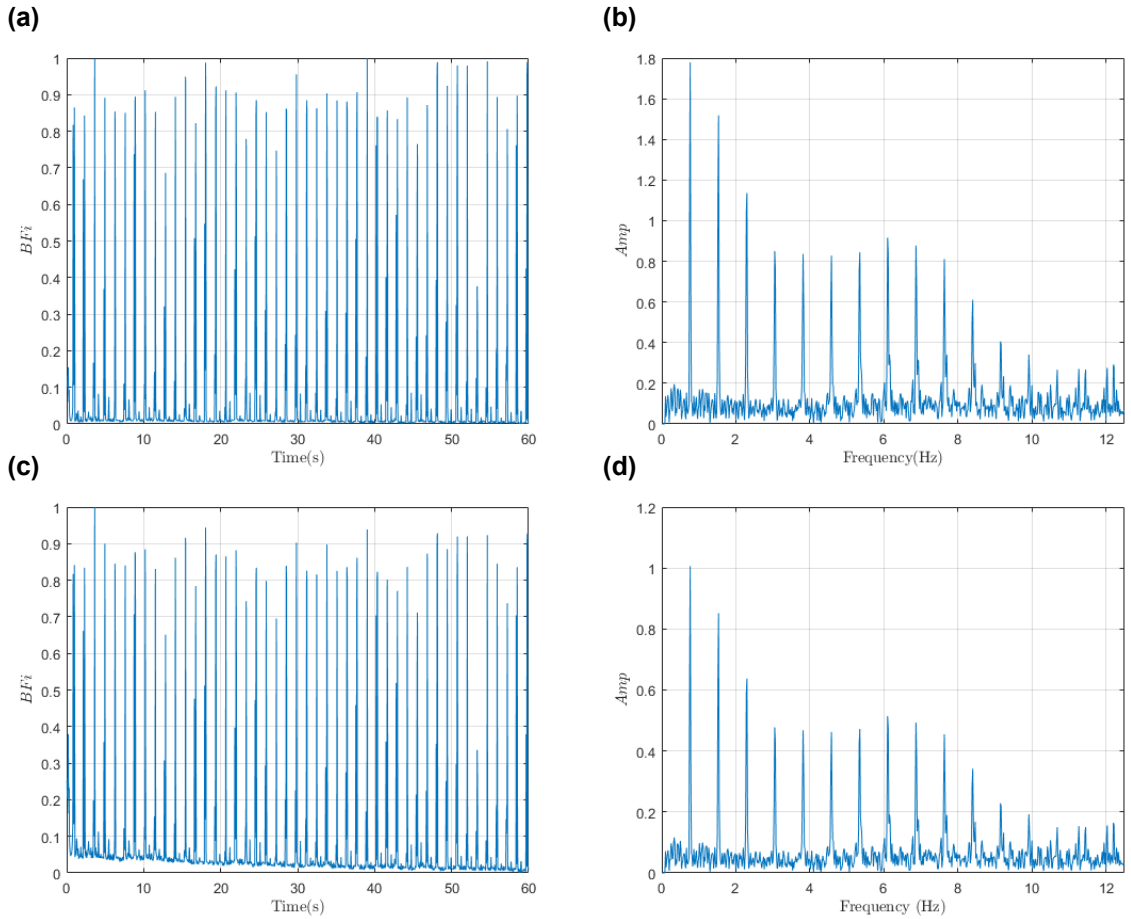

Figure B.1: Comparison of ISVS and LSCI performance at maximum SNR (D = 9 cm) for 1.5 cm phantom: (a,b) ISVS time and frequency domain; (c,d) LSCI time and frequency domain.

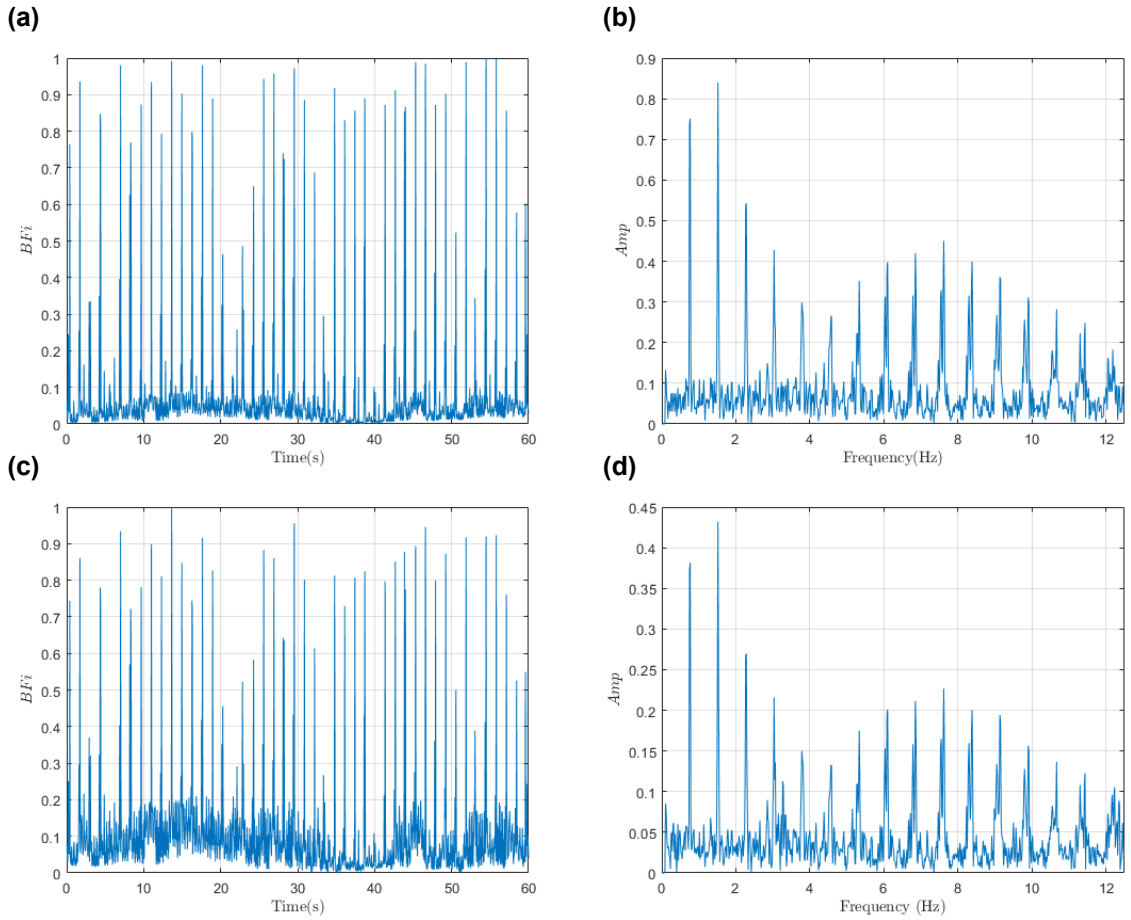

Figure B.2: Comparison of ISVS and LSCI performance at the furthest measurable depth (D = 18 cm) for 1.5 cm phantom: (a,b) ISVS time and frequency domain; (c,d) LSCI time and frequency domain.

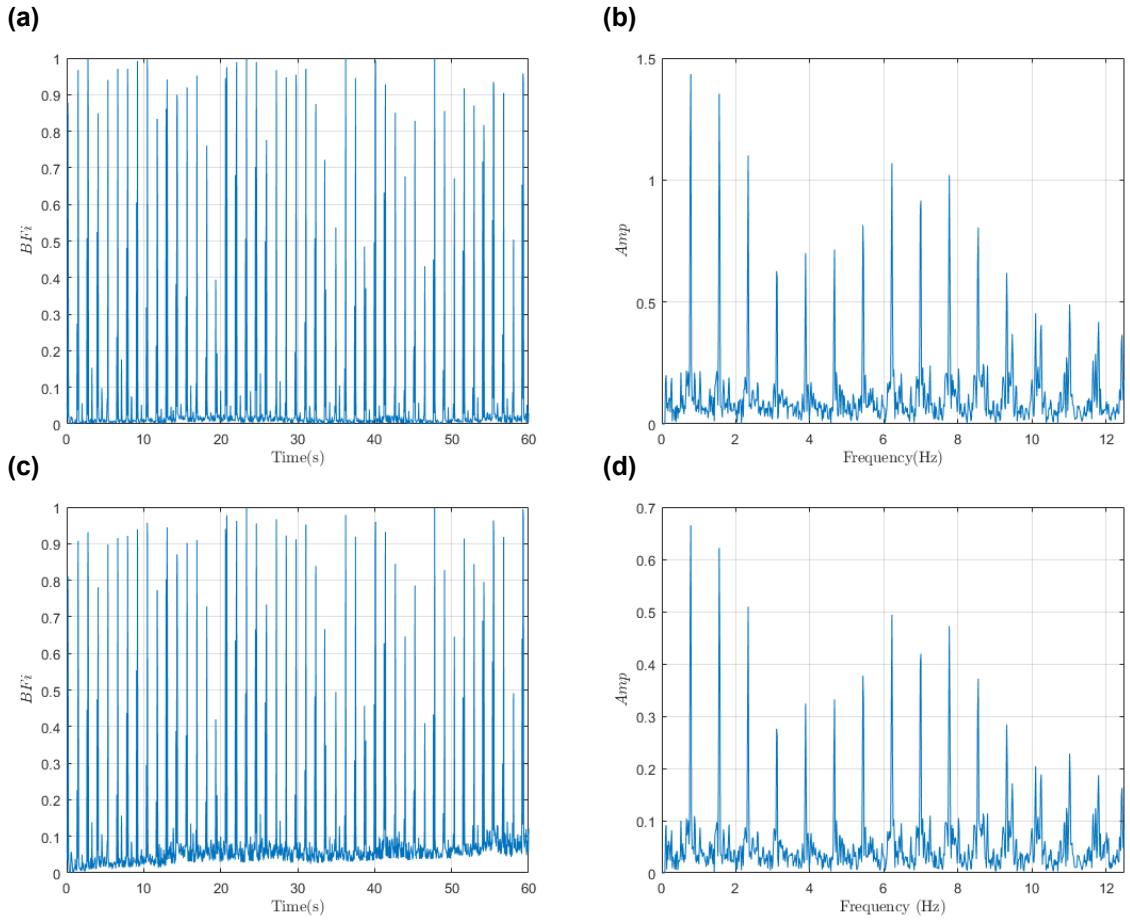

Figure B.3: Comparison of ISVS and LSCI performance at maximum SNR (D = 10 cm) for 2 cm phantom: (a,b) ISVS time and frequency domain; (c,d) LSCI time and frequency domain.

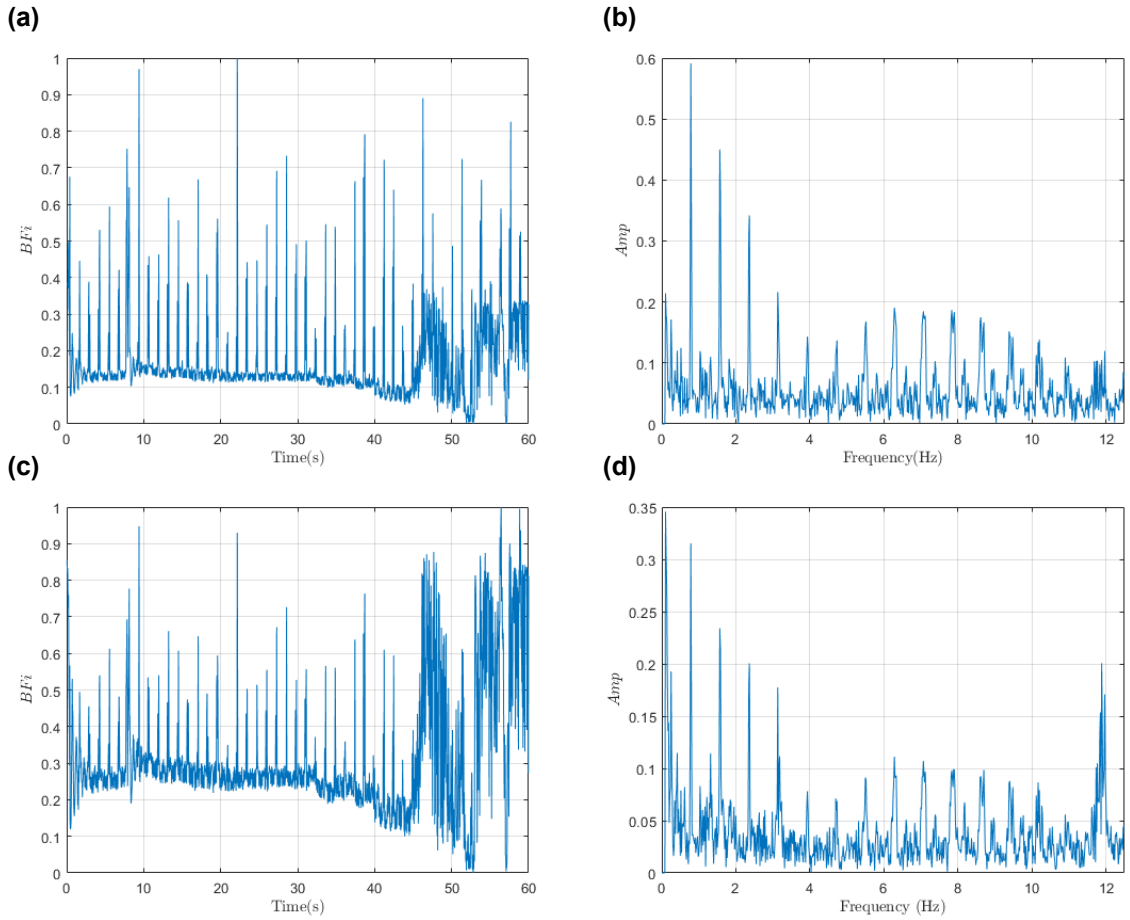

Figure B.4: Comparison of ISVS and LSCI performance at the furthest measurable depth (D = 17 cm) for 2 cm phantom: (a,b) ISVS time and frequency domain; (c,d) LSCI time and frequency domain.